Contourite-like deposits suggest stronger-than-present circulation in the Plio-Pleistocene Red Sea

Neil C. Mitchell [a,*], Marco Ligi [b], Jonas Preine [c], Diederik Liebrand [a], Moamen Ali [d], Alessandro Decarlis [d]

[a] Department of Earth and Environmental Sciences, University of Manchester, Williamson Building, Oxford Road, Manchester M13 9PL, UK
[b] Istitutodi Scienze Marine, CNR, Via Gobetti 101, 40129 Bologna, Italy
[c] Institute of Geophysics, Universität Hamburg, Mittelweg 177, 20148 Hamburg, Germany
[d] Department of Earth Science, Khalifa University, Earth Sciences Department, P.O. Box 127788, Abu Dhabi, United Arab Emirates

ARTICLE INFO

ABSTRACT

Red Sea Deep Water is presently slow-moving, but was this true of the earlier Plio-Pleistocene (PP)? In seismic reflection records, the PP deposits are distorted by halokinetic deformation of their underlying Miocene evaporites. However, if reflections are flattened to a prominent reflector representing the top of the Miocene, they reveal mounded deposits within the earlier PP along both sides of the sea. Off Egypt, a plastered drift occurs along a salt wall. In the central Red Sea, they are mounded drifts. Seismic reflections from these deposits change shape gradually upwards to the modern seabed, which is commonly flatter, suggesting a gradual change in depositional conditions. To explain their origins, we appeal to other evidence. DSDP cores from the Late Pleistocene contain the rigid aragonite cements formed by restricted conditions, but not the lower and middle PP. Furthermore, mid-PP sedimentary δ^{18}O values are similar to global ocean δ^{18}O for that time, not enhanced as expected from excess evaporation. These data suggest that there was a greater exchange of Red Sea waters with the Indian Ocean during the mid-PP. That exchange may have allowed waters densified by evaporation in shallow regions of the northern Red Sea to flow south vigorously (the mounds would then be contourites). Alternatively, as the Pliocene seabed was shallower, wind-driven eddies may have affected more of the water column. Overall, the results indicate for the first time that deep circulation was stronger in the earlier PP compared with the present day. That circulation needs to be considered when evaluating organism dispersions across the Red Sea, regional climate, and influence of Red Sea Outflow Water on Indian Ocean Intermediate Water.

Plain language summary: During the Pliocene (about 3–5 million years ago), temperatures on Earth's surface were similar to those predicted in some models of Earth's future climate. This has led to researchers becoming interested in studying geological evidence of conditions during the Pliocene as a clue to Earth's future. In detail, however, the comparison may not be exact. In our article, we describe mounds of sediment that were originally formed on the bed of the Red Sea in the Pliocene. They appear similar to snow drifts, and like snow drifts, may have formed under steady currents. Sea water becomes dense with evaporation (making it more saline). At the present day, dense water created in the Gulf of Suez cascades down into the deep Red Sea as a slow current. Perhaps such movements were more vigorous in the Pliocene, helped by the water escaping through a deeper barrier in the south into the Indian Ocean? Alternatively, these mounds were formed by giant eddies, such as those on the surface of the modern Red Sea, which are moved by strong winds. In either case, the deep waters of the Pliocene Pliocene Red Sea were more vigorously moving compared to the quiescent deep waters of the modern-day.

1. Introduction

The Red Sea contains some of the world's hottest and saltiest seawater. Its deep water is presently sluggish, moving at speeds of <1 cm/s (Sofianos and Johns, 2007). One of the reasons for this sluggishness is the small connection to the Indian Ocean through the Bab el Mandeb Strait (Fig. 1), which limits water exchange between these two water bodies and thus leads to strong density stratification (Maillard and

Soliman, 1986). Evaporation in the regional desert climate, coupled with reduced replenishment of water of more normal ocean salinity from the Gulf of Aden, has caused the sea to become unusually saline (>40‰ (Cember, 1988)). Much of the oceanographic interest in the sea has centred on its unusual features, such as the dynamics of flow through the Bab el Mandeb Strait (located in Fig. 1) (Lane-Serff et al., 2000; Smeed, 2000; Smeed, 2004). In the subject of Palaeoceanography, researchers have been concerned with how high evaporation rates and the limited
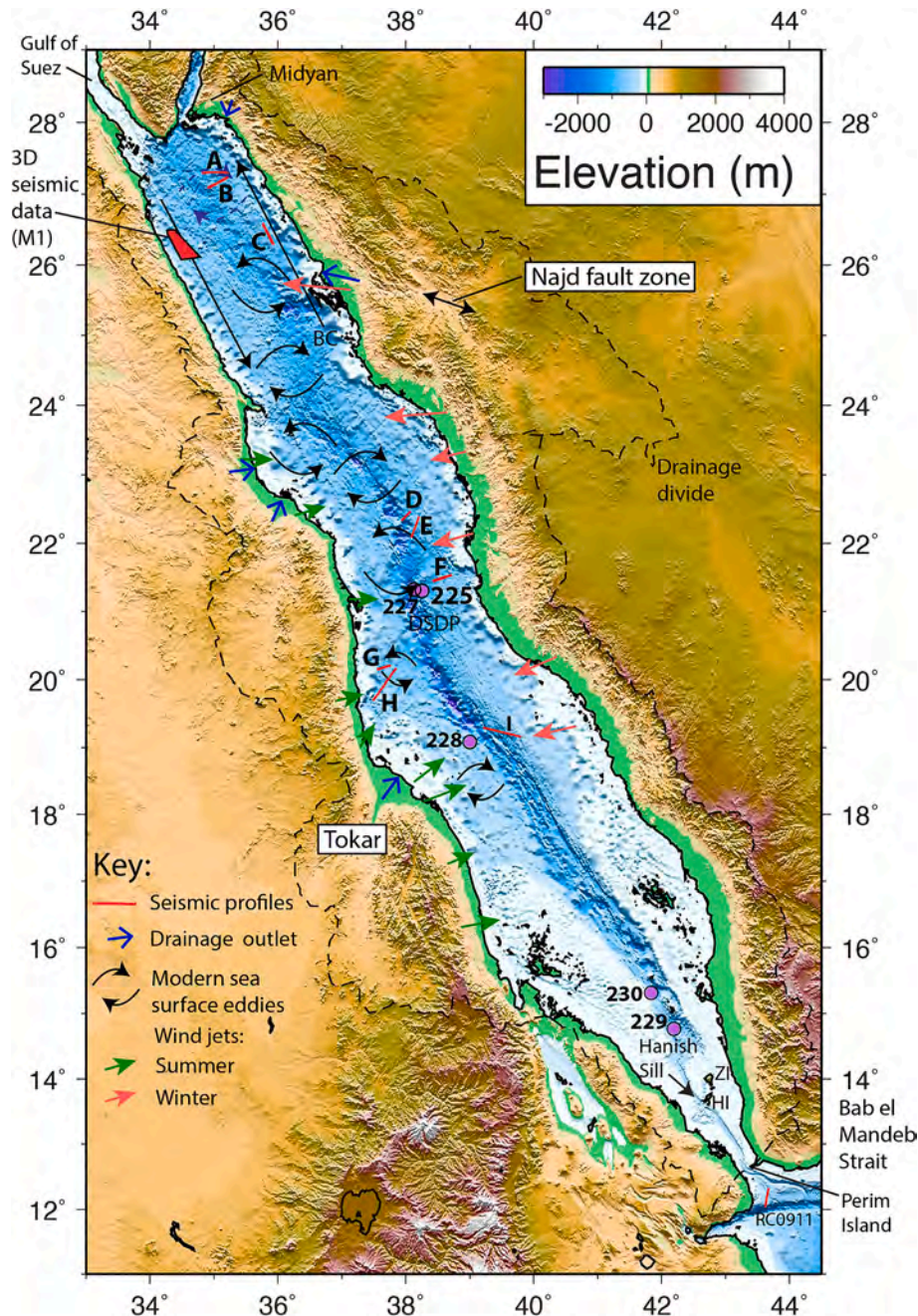
Fig. 1. Bathymetry and elevations of the Red Sea (data of Becker et al. (2009) obtained from topex.ucsd.edu). Data from red polygon marked "3D seismic data" are shown in Fig. 6. Red lines marked A-I locate profiles shown in Fig. 7. Purple-filled circles with bold numbers 225–230 locate five Deep Sea Drilling Project sites (Whitmarsh et al., 1974). Green and Red arrows on either side of the Red Sea represent seasonal transverse wind jets, which modify the mostly north-northwesterly winds (Jiang et al., 2009). Blue arrows locate outlets of fluvial systems that drain the continental interiors beyond the Red Sea Hills (Mitchell et al., 2019). Circulating arrows locate seven clusters of eddies occurring between January 2018 and November 2019 obtained by clustering and hotspot analysis by Campbell (2020), his Fig. 4.8. A further weaker cluster of anticyclonic eddies is located by dark blue dashed curves at A and B annotation. Dashed irregular line is the drainage divide around the Red Sea derived from Hydrosheds (www.hydrosheds.org; Lehner and Grill, 2013). HI: Hanish Island, ZI: Zukur Island. Hanish Sill is the shallowest point separating the Red Sea from the Gulf of Aden. BC: boundary current of Sofianos and Johns (2003) (straight NNW vector, with corresponding weaker SSE current vector on west side of Red Sea). (For interpretation of the references to colour in this figure legend, the reader is referred to the web version of this article.)

sea connection have led to a higher proportion of the isotope ^{18}O compared with ^{16}O in its waters, which are recorded in shallow-buried carbonates (Hemleben et al., 1996). As the exchange flow is affected by water depth over Hanish Sill (the shallowest point between the Red Sea and Gulf of Aden basins), which is itself modulated by global sea-level, modelling of that exchange has allowed Late Pleistocene relative sea-level to be reconstructed from sedimentary oxygen-isotope data (Siddall et al., 2004; Grant et al., 2014; Rohling et al., 2014).

At present, the Red Sea has modest impact on waters outside the basin, although its outflow, combined with densified waters from the Persian Gulf, contributes to a > 1 km thick intermediate water body in the Indian Ocean (Kawagata et al., 2006). Remnants of its high salinity appear 6000 km from the Red Sea within the Agulhas Current (Beal et al., 2000). During the early Holocene, a more saline Red Sea outflow affected deeper Indian Ocean waters (Jung et al., 2001). If the Red Sea were more open to the Gulf of Aden and Indian Ocean in the Pliocene and earlier Pleistocene, its outflow may have affected Indian Ocean waters differently in ways that are difficult to anticipate. Furthermore, the distance between Arabia and Africa around the Bab el Mandeb Strait is presently small (Fig. 1) and there is evidence of it being only a minor barrier for mammal dispersions in the Pleistocene (Winney et al., 2004; Kopp et al., 2014). During the Last Glacial Maximum (LGM), some seaways around the Strait may have been only 1–3 km wide, making the region a potential route for hominin dispersions from Africa onto Arabia (Lambeck et al., 2011). However, if the Bab el Mandeb Strait were broader in the earlier PP, it may have been a more effective impediment to the dispersions of mammals and other organisms. These include earliest hominins, whose remains have been found in Eurasia at Dmanisi, Georgia (1.8 Ma; Garcia et al., 2010; Messager et al., 2011), and other evidence in the Siwaliks, India (2.6 Ma; Dambricourt Malassé, 2016) and on the Chinese Loess Plateau (2.1 Ma; Zhu et al., 2018). A barrier in the southern Red Sea would favour the northern dispersion route across Sinai and the Levant (Bar-Yosef and Belfer-Cohen, 2001; Ron and Levi, 2001; Eppelbaum and Katz, 2022). Thus, knowledge of the past Red Sea circulation may have implications beyond merely the basin sediments.

Elongate mounds in the PP sediments off the coast of Egypt have been identified previously (Mitchell et al., 2019). We further investigate those features and, using legacy shallow seismic reflection data, identify other elongated mounds of sediment. These sediments were deposited on a highly mobile substrate of Miocene evaporites, which are widespread beneath the Red Sea (Mitchell et al., 2022). If allowance is made for the halokinetic deformation, the reflections from the earlier PP can be shown to contain mounds that originally had geometries similar to those of contourites (Viana et al., 1998; Faugères et al., 1999; Rebesco et al., 2014; Hernández-Molina et al., 2016). Although some of the seismic reflection data shown here were recorded onto paper only (and hence are of lower quality than seismic data recorded with modern digital methods), they suggest similar mound-like geometries occurring over various parts of the Red Sea (Fig. 1). The article first includes an extensive background section on aspects of the Red Sea deep-water sediments and regional paleoclimate and paleoceanography existing over the PP. It then focuses on observations of the mounds in the seismic data and their interpretation given the halokinetics. Deep-water mounded deposits may represent contourites formed by thermohaline circulation, but they may have other origins (Shanmugam, 2017). The discussion section therefore draws together evidence from the seismic data and the extensive background section to assess their origins, principally thermohaline and wind-driven circulations. The combined information and our discussion indicate that conditions were markedly different in the earlier PP compared with the upper Pleistocene and Holocene.

2. Background

2.1. Deep-water sediments recovered at Deep-Sea Drilling Project (DSDP) sites

Some information on the PP deep-water hemipelagic sediments and their environment was provided by the sampling at DSDP Sites 225, 227, and 228 (Fig. 1) (Whitmarsh et al., 1974). Sampling was carried out by rotary drilling and recovered only 1/3 to 2/3 of the stratigraphy at each site, but the reports based on it are valuable as they are the only deep-water samplings of the lower Pleistocene and Pliocene publicly available. Fig. 2 summarises some of the information, including sediment texture (Bode, 1974a), carbonate contents (Bode, 1974b), sediment biostratigraphic dates updated to modern chronologies (www.geomapapp.org; WBF Ryan, pers. comm., 2009), the units assigned by shipboard scientists (Whitmarsh et al., 1974), and rigid aragonite/Mg-calcite-rich layers (Stoffers and Ross, 1974). Stoffers and Ross (1974) described the units at Site 225 as ("micarb" representing carbonate of small grain size): Unit 1, micarb-rich detrital clay-silt nanno ooze and chalk, Unit 2, micarb-rich nanno detrital silty claystone, Unit 3, dolomitic silty claystone. At Site 227, they were described slightly differently as: Unit 1, micarb-rich detrital clay nanno ooze and chalk, Unit 2, micarb-rich detrital nanno silty claystone, Unit 3, dolomitic silty claystone. The units at Site 228 were described as: Unit 1, detrital silt-rich micarb nanno ooze and micarb-rich siltstone, Unit 2, micarb siltstone, Unit 3, dolomitic detrital silty claystone. Unconformities were interpreted between the Pliocene and Pleistocene at Sites 225 and 227 (Stoffers and Ross, 1974; Whitmarsh et al., 1974).

Carbonate contents increase systematically from low values to ~60% on average up-section at Site 225 and 227 in Fig. 2, whereas no systematic variation is observable for Site 228. Site 228 lies close to the Tokar Delta (Fig. 1), so terrigenous sediments from that area complicate interpretation of carbonate contents for that site (Stoffers and Ross, 1974; Whitmarsh et al., 1974). The variations for Sites 225 and 227 might be interpreted as being caused by increasing carbonate saturation (hence leading to inorganic aragonite precipitates (Milliman et al., 1969; Rohling et al., 1998)). Increasing carbonate saturation could be a sign of increasing isolation of the Red Sea waters from the global ocean. Alternatively, the trend may simply be an artifact of decreasing dilution by the non-carbonate (largely terrigenous) component. We address this below by calculating mass accumulation rates of the carbonate and non-carbonate fractions separately.

The evaporitic sediments recovered at Sites 225, 227 and 228 below the Plio-Pleistocene sediments comprise mainly inter-bedded halite, anhydrite and shale (Whitmarsh et al., 1974). Seismic reflection data typically show areas of either layered reflectivity or transparency (Izzeldin, 1987). The former has been suspected to correspond with the layered evaporites found at the drill sites, while transparent areas represent more massive halite (Izzelatin, 1987; Colombo et al., 2014; Mitchell et al., 2017; Delaunay et al., 2023). Consequently, seismic reflection images reveal evidence for extensive diapirism (Ross and Schlee, 1973; Izzeldin, 1987; Davison et al., 1994; Rowan, 2014; Delaunay et al., 2023). However, in deep waters the diapirism is mostly at a less developed "pillow" stage, possibly because the sediments between diapirs have low densities (Mitchell et al., 2010; Mitchell et al., 2022). Hence, the deep-water stratigraphy has not been inverted into allochthonous sheets and the units there still lie in depositional order.

2.2. Modern oceanography

According to Cember (1988), Red Sea Deep Water (RSDW) originates from waters densified by evaporation in the shallow Gulf of Suez and other areas in the furthest north of the Red Sea, with a renewal rate of 0.16 Sverdrup (1 Sv = 10^6 m^3/s) and a residence time of 36 years. In the north, RSDW flows southwards, presumably with a current of ~0.16 Sv. To give a sense of scale, if that discharge were uniformly distributed over
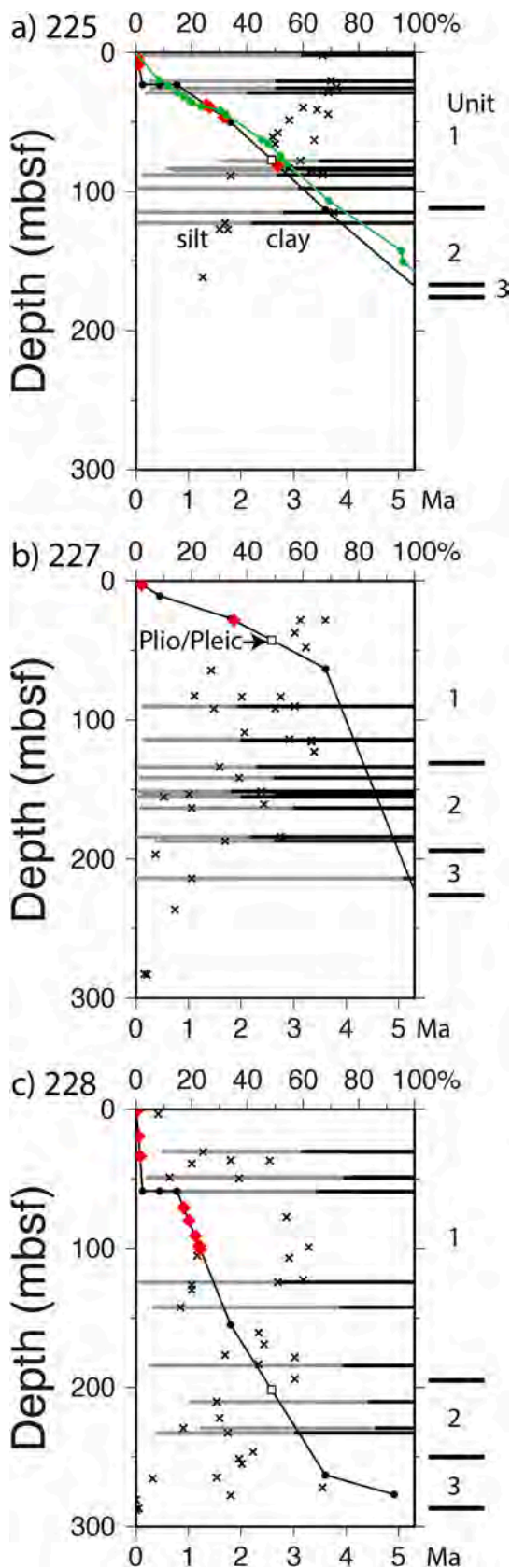
Fig. 2. Data from the three DSDP sites located in Fig. 1. Grey-scale bars represent the results of grain size measurements made on selected cores (Bode, 1974a) (white, grey and black representing % sand, silt and clay). Carbonate contents (%) are indicated by x-symbols using the same scale as the grain sizes. Lines show the sediment age models for these sites obtained from stratigraphic data (solid black circles connected by solid lines) updated to modern ages provided within the GeoMapApp data browser (www.geomapapp.org; WBF Ryan, pers. comm., 2009). In top panel, green circles and green line show alternative depth-age model for Site 225 (Hughes and Varol, 2024). Open squares are the positions of the Pliocene-Pleistocene boundary at 2.58 Ma (Rio et al., 1998). Red diamond symbols show the depth distribution of lithified aragonite and magnesium-calcite according to Stoffers and Ross (1974). Note units assigned by the shipboard scientists (Whitmarsh et al., 1974) are based on sediment properties and do not have equal age ranges. (For interpretation of the references to colour in this figure legend, the reader is referred to the web version of this article.)

the ~100 km² cross-section of the Red Sea below 200 m depth, it would imply a current of only 1.6 mm/s. Cember (1988) also speculated that dissolution of halite from the seabed could be contributing to densification of RSDW. The salinity reaches >40‰ in the Red Sea because of only weak exchange with waters in the Gulf of Aden through Bab el Mandeb Strait (Maillard and Soliman, 1986; Pratt et al., 1999; Smeed, 2004) and a strong density stratification preventing wind-driven overturning. The stratification is illustrated by potential densities (densities corrected for pressure), which increase with depth (Jarosz et al., 2005) and oppose upwelling of RSDW. Red Sea Outflow Water (RSOW) with a potential density of ~1028.0 kg/m³ overlies RSDW with a potential density of ~1028.6 kg/m³ (Sofianos and Johns, 2003). The boundary between the two water bodies lies at ~200 m. Consequently, RSOW originates from intermediate depths in the Red Sea (Neumann and McGill, 1962; Cember, 1988; Sofianos and Johns, 2003).

In winter, RSOW is expelled in a bottom layer across Hanish Sill (Fig. 1) while overlying less saline Indian Ocean water enters the Red Sea in a shallow surface layer to balance the outflow and evaporation losses (Lane-Serff et al., 2000). During summer, when a northwesterly wind replaces the winter southeasterly wind (Jiang et al., 2009), a three-layer water structure can develop, with Gulf of Aden Intermediate Water intruding over the sill between outflowing surface water and RSOW. The winds are dominantly from the northwest to southeast along the basin, except in winter when the southerly half experiences winds from the south (Jiang et al., 2009). These winds shape the general circulation, so that the incoming fresher Indian Ocean water forms a northwestward-flowing boundary current along the west side in the southerly Red Sea, switching over to the east side along the northern half of the basin (Sofianos and Johns, 2003; Zhai and Bower, 2015).

In summer, the winds have westerly components originating from wind gaps in the western Red Sea Hills, in particular, through the Tokar area (Fig. 1; Jiang et al., 2009). In winter, winds are instead modified by components flowing through the mountains on the eastern side of the sea. The seasonal cross-sea airstream components partly cause ephemeral eddies to form on the sea surface spanning the Red Sea almost to both coasts (Quadfasel and Baudner, 1993; Zhai and Bower, 2013; Chen et al., 2014; Bower and Farrar, 2015; Nicholls et al., 2015). On the other hand, some eddies form in ocean general circulation models without these cross-basin winds (Clifford et al., 1997; Biton et al., 2008), likely because of the important effect of water buoyancy (Sofianos and Johns, 2003). Shipboard acoustic Doppler current meter (ADCP) data show that such circulation is confined to the surface waters and is negligible (<1 cm/s) below 200–300 m depth (Sofianos and Johns, 2007; Chen et al., 2014). Fig. 1 locates seven sites where eddies repeatedly occurred, detected from satellite altimetry between January 2018 and November 2019 (Campbell, 2020).

2.3. Paleoceanography of the Red Sea in the late Pleistocene

Many shallow-penetrating sediment cores have been collected in the deep waters of the Red Sea and analysed, providing a continuous stratigraphy as far as back as ~500 ka (Grant et al., 2014). During the Late Pleistocene, lowering of global mean sea-level during glacial periods restricted the exchange of water with the Gulf of Aden, leading to the Red Sea becoming more saline and to rigid sedimentary layers forming from inorganic aragonite precipitation (Milliman et al., 1969; Almogi-Labin et al., 1996). Near-surface reflections observed in high-resolution CHIRP seismic records are produced by those layers and have been interpreted as showing that aragonitic layers have formed at least since Marine Isotope Stage 16 at ~620 ka (Mitchell et al., 2015). ("CHIRP" is short for "Compressed High-Intensity Radar Pulse", the type of seismic source used (Schock et al., 1989).) During glacial times, some benthic foraminifera and pteropods survived, suggesting that the Red Sea did not become completely disconnected from the Gulf of Aden and thus hypersaline (Almogi-Labin et al., 1998; Fenton et al., 2000). Glacio-isostatic modelling results suggest that, during the Last Glacial Maximum (LGM), water depth at the shallowest part of Hanish Sill (Fig. 1) averaged 13 ± 4 m, with a maximum of 25 ± 4 m (Lambeck et al., 2011). Pelagic-sediment δ^{18}O values through the LGM remained compatible with continuous though restricted exchange with the Gulf of Aden (Siddall et al., 2003; Siddall et al., 2004; Biton et al., 2008; Rohling et al., 2009). Reflections corresponding with Marine Isotope Stage 12 (~450 ka) in CHIRP seismic data collected in the central Red Sea mostly drape their underlying reflections and suggest a lack of current-modified sediment deposition (Mitchell et al., 2019). The present quiescent RSDW conditions have therefore likely persisted since at least 450 ka.

2.4. Paleoceanography of the Red Sea through the Plio-Pleistocene (PP)

The earlier PP is more poorly known. Because an Indian Ocean fauna is found in early Pliocene sediments throughout the Red Sea (Swartz and Arden, 1960; Purser and Hötzl, 1988; Orszag-Sperber et al., 1998b), the sea was then connected to the Gulf of Aden. The isotopic data shown in Fig. 3 were derived from two sets of measurements on samples from the
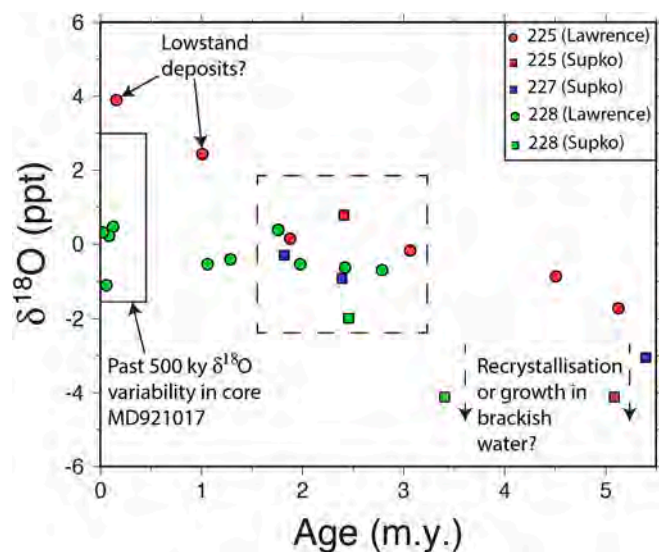

Fig. 3. Measurements of δ^{18}O (relative to the PDB standard) on bulk carbonate (Lawrence, 1974) and calcite (Supko et al., 1974). Also shown (upper rectangle) is the range of δ^{18}O measured on *Globigerinoides ruber* tests from core MD921017 (Rohling et al., 1998). The measurements of Lawrence (1974) have been converted to the PDB standard using the Coplen et al. (1983) relation. The data within the dashed rectangle have a mean of -0.39‰ and standard deviation of 0.73‰. (A colour version of this figure can be found on the online version of this article.)

DSDP cores. Those of Lawrence (1974) were on bulk carbonate fractions. Supko et al. (1974) measured δ^{18}O on calcite in the presence of dolomite, attempting to separate oxygen from the two minerals by measuring gas emitted with progressive reactions with acid. Given the few biostratigraphic constraints used to construct the age models, and differences for DSDP Site 225 with those of Hughes and Varol (2024) (Fig. 2), ages are probably uncertain by ~0.5 m.y. Bearing age uncertainties in mind and that these bulk measurements obscure isotopic variations between species, however, there are ostensibly sensible aspects to the variations in δ^{18}O with age. For example, the δ^{18}O range for sediments younger than 1.5 Ma are broadly compatible with δ^{18}O measured on *G. ruber* tests for the past 500 ka, which vary from -1 to $+3$‰ (Rohling et al., 1998). Extreme high ^{18}O/^{16}O ratios occur in tests deposited during lowstands of global sea level when restricted exchange at Hanish Sill led to greater ^{18}O/^{16}O ratio in Red Sea waters arising from more evaporative loss of ^{16}O. We interpret the two values marked in Fig. 3 as due to such lowstands, although the value at ~200 ka of $+3.9$‰ is higher than $+3$‰ extreme lowstand values (Rohling et al., 1998), suggesting an uncertainty of at least 1‰ in these older measurements.

At greater depth and sediment age, low δ^{18}O occurrences at the right of the graph have been suggested to be due to exchange of oxygen during recrystallisation (Lawrence, 1974). Between upper 500 ka and the 3–5.3 Ma, the δ^{18}O values vary little; the standard deviation for data within the dashed rectangle in Fig. 3 is 0.73‰. For comparison, we calculated a standard deviation of 0.54‰ for the 1.5–3.0 Ma interval of benthic foraminifera measurements at Ceara Rise in the Atlantic Ocean (Wilkens et al., 2017). Recrystallisation in situ does not obviously explain the narrow range of δ^{18}O in the DSDP sample data, given the more extreme values present elsewhere in the stratigraphy that are preserved and arguments of Lawrence (1974). The possibility of these sedimentary δ^{18}O values being contaminated by modern ocean values is also unlikely given that sodium chloride concentrations in interstitial water are concave upwards (Manheim, 1974) and readily modelled with upwards water advection (Ranganathan, 1991). ^{18}O may be fractionated during inorganic co-precipitation of dolomite and calcite by 2.3–4.0‰ between the minerals, in favour of dolomite (Chacko and Deines, 2008, their Fig. 7), but the calcite values in Fig. 3 are not systematically different from the bulk carbonate values. Given their similarity with open ocean values, the modest δ^{18}O values of the mid-PP and their small variability are likely due to efficient exchange of water with the Gulf of Aden preventing extremes in isotopes occurring (Lawrence, 1974).

The diversity of foraminiferal fauna is generally low in the PP compared to open-ocean faunas and varied pelagic faunal content of the early Pliocene suggest rapidly fluctuating conditions in the inhabited sea surface waters then (Fleisher, 1974). In Fig. 4, we show the abundances of selected pelagic foraminifera for DSDP Sites 225 and 228 estimated by Akers (1974) (see figure caption for details), chosen as they are more abundant and their environmental sensitivities were summarised by Fenton et al. (2000). In Fig. 4, these species were all absent or found in extremely low abundances at the start of the Pliocene. Abundances remained modest throughout the Pliocene, increasing gradually in some cases (e.g., *G. ruber*) towards the Pleistocene. From Fenton et al. (2000), *G. sacculifer*, *G. ruber*, and *G. siphonifera* tolerate salinities of 24–49‰, 22–49‰ and 27–45‰. Caruso et al. (2013) interpreted a "Lago-Mare" stage of low salinity and hypoxic conditions from the restricted fauna and from their own δ^{18}O data for the earliest Pliocene at Site 225 (such effects are also observed in the Mediterranean "Lago-Mare" deposits (Pierre et al., 2006)). The lower-Pliocene negative δ^{18}O values in Fig. 3 and other data of Caruso et al. (2013) would be compatible with rain-water input, so we accept their revised interpretation of low salinity in the early Pliocene.

2.5. Lithologies indicative of high salinity suggested by seismic reflection data

In seismic reflection data collected away from coasts and hence more
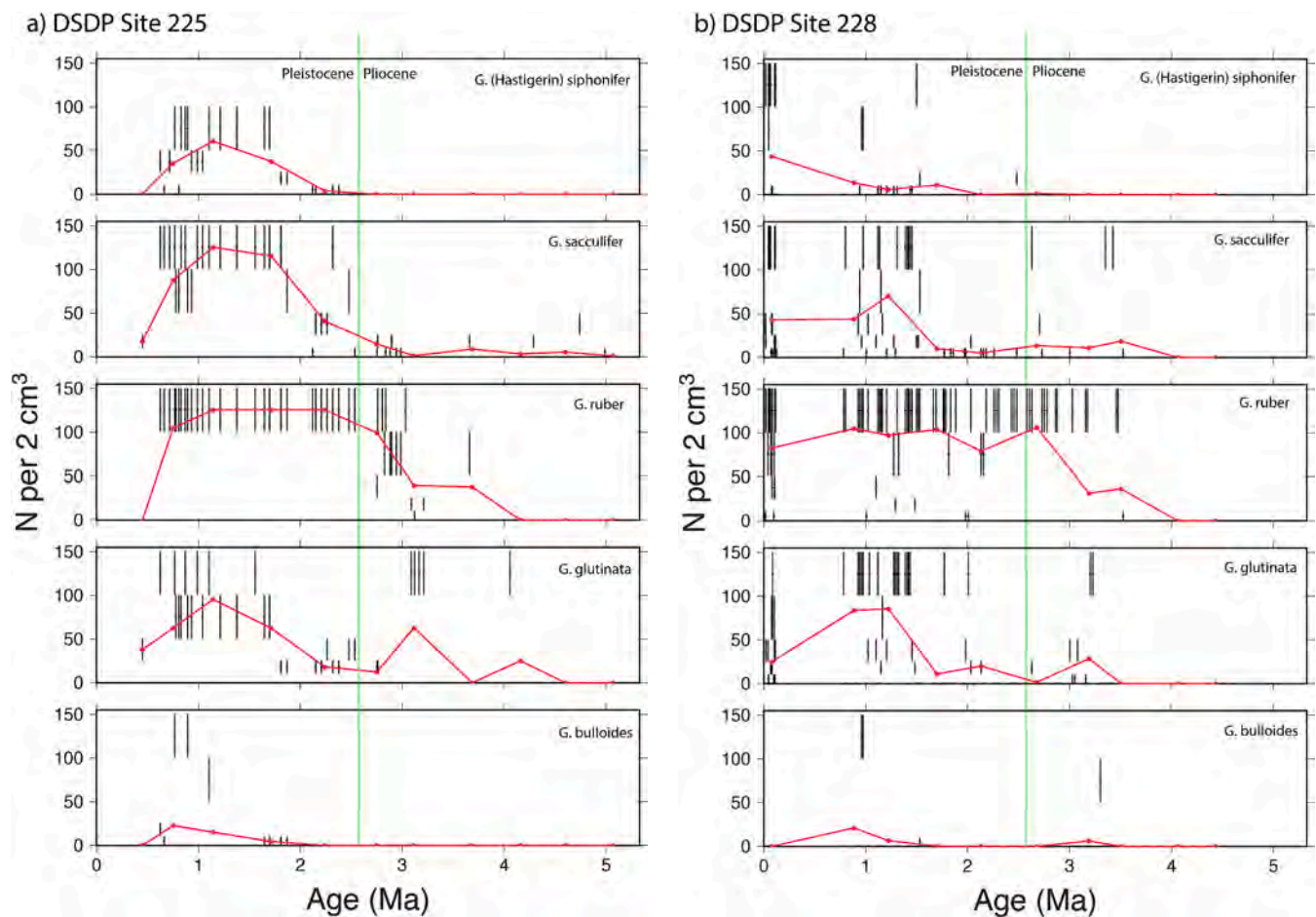
Fig. 4. Species counts for each 2 cm^3 sample analysed by Akers (1974). Akers (Akers, 1974) reported abundances as estimates within ranges in six groups: 0, 1–10, 11–25, 26–50, 51–100 and > 100. For the last group, we have assumed the equivalent range 100–150. The graphs show those ranges as vertical bars, along with their central value (small solid circles). Averages of those central values, including zero counts where species were absent, were computed every 0.5 m.y. and are shown by the red lines. In (a), the age-depth model of Hughes and Varol (2024) for DSDP Site 225 has been used. In (b), the age-depth model is from GeoMapApp (www.geom apapp.org). In both graphs, the vertical green lines mark the Plio-Pleistocene boundary from the DSDP reports (Whitmarsh et al., 1974). (For interpretation of the references to colour in this figure legend, the reader is referred to the web version of this article.)

remote from terrigenous sediment sources, the lower hemipelagic PP is commonly transparent, an observation that has been interpreted as due to a lack of inorganic aragonite cemented layers and thus lack of isolation events caused by global sea-level lowerings (Mitchell et al., 2015). The transparency would be consistent with a lack of seismic impedance variation over sediment depth intervals equal to or greater than a quarter of a seismic wavelength (a few metres for these data). Seismic impedance equals density times seismic velocity, both of which would be elevated if rigid cements were abundant. Aragonite/Mg-calcite-rich layers are also absent in the lower-PP DSDP cores (Fig. 2) (Stoffers and Ross, 1974). The lack of such layers supports the view that the sea was more freely exchanging water with the global oceans during the mid-PP and had low salinity due to the freshwater inputs in the early Pliocene, both consistent with our interpretation of the δ^{18}O data.

2.6. Changing basin physiography

The sea was much shallower on average at the start of the Pliocene because it has since then deepened with lithospheric thermal subsidence and deflation of the evaporite surface due to the evaporites flowing towards the oceanic spreading centres (Augustin et al., 2016; Mitchell et al., 2017). Mitchell et al. (2021) attempted to quantify how those and other factors affected the evaporite surface level. They measured the present elevation of the evaporite surface as 908 m below modern sea level (bmsl) on average from deep seismic data over the flanks of the

central Red Sea. These were selected to be away from coasts and away from the central deeps (topographic depressions containing volcanic geomorphological structures). After correcting for the above factors, at the start of the Pliocene, the evaporite surface was estimated to have lain ~192 m below modern sea level if the basin were water-filled at that time. In practice, the Red Sea may have become fully isolated and drawn down at about the Miocene-Pliocene boundary, even if only briefly, as an unconformity is commonly observed at the seismic "S" reflection near the top of the Miocene evaporites (Izzeldin, 1987; Mitchell et al., 2017; Mitchell et al., 2021; Delaunay et al., 2023).

A clue to past physiography of the basin axis can also be gleaned from geophysical data. Oceanic sea-floor spreading likely began at ~10 Ma in the central Red Sea (Mitchell et al., 2021), based on the lateral extent of symmetrical magnetic anomalies (Okwokwo et al., 2022; Delaunay et al., 2023) and changes in relationships between basement depth and gravity anomalies (Shi et al., 2018). The magnetic anomalies change character from low frequency on crust older than ~5 Ma to normal high-frequency sea-floor spreading anomalies on crust <5 Ma. This change suggests exposure of spreading centres to seawater (hence more typical oceanic anomalies) as sea-floor spreading outpaced the movements of the evaporites (Okwokwo et al., 2022). If spreading centres were exposed to sea water, their depths can be expected to have followed those of spreading ridges globally, as they are largely dictated by isostatic balance over Earth's asthenosphere (Klein and Langmuir, 1987). The presence of "normal" sea-floor spreading on crust younger

than 5 Ma therefore implies that the Pliocene central Red Sea had deeps along its centre, perhaps reaching the ~2000 m depth of the present spreading centres. However, as the evaporites were likely more extensive then (Okwokwo et al., 2022), we suspect those deeps were more isolated than at the present day and more like those of the modern northern Red Sea (Cochran, 2005). Hence, they may not have played a major role in RSDW circulation.

2.7. Regional climate of the Plio-Pleistocene

Variations in air temperature, humidity, and winds were all potentially important for evaporation and circulation in the Red Sea (as wind stress affects the water surface directly, whereas salinity changes caused by evaporation affect water buoyancy relative to the Indian Ocean waters). We therefore review the limited evidence on these aspects available for the PP. Dowsett et al. (2013) compiled sea-surface temperatures for the Pliocene. Their sample sites nearest the Red Sea were modestly warmer than present (<2 °C) based on foraminifera (sites in Italy and DSDP Site 722 off the coast of Oman), whereas one site on Crete suggested modestly cooler temperatures by a similar amount. Such data from sites near coasts are difficult to interpret as sea surface temperatures can be affected by wind-driven upwelling. Liddy et al. (2016) reported measurements of an organic proxy for sub-surface water temperature on samples from DSDP Site 231 in the Gulf of Aden. Their results suggested that early Pliocene temperatures were similar to those of the modern ocean and that a ~ 5 °C cooling subsequently occurred from 5 to 2 Ma. Their measurements of hydrogen and carbon isotopes in plant wax and pollen data suggest that the northeast African climate in the early Pliocene was generally wetter than today (grassland) but became drier towards the late Pliocene (more arid-adapted shrubland).

During some intervals of the Pleistocene, the region was wetter than today; evidence includes lake deposits in locations that are presently arid (Rosenberg et al., 2013; Matter et al., 2015; Nicholson et al., 2020). These "pluvial" intervals are also inferred from speleothems from Yemen (Fleitmann et al., 2011), Egypt (Rifai, 2007) and Israel (Bar-Matthews et al., 2003; Vaks et al., 2006; Vaks et al., 2010; Vaks et al., 2013). Intermittent wet climates also likely occurred in the Pliocene, when largely savannah, steppe, and grassland surrounded the Red Sea (Dowsett et al., 1994). For example, arboreal pollen found within boreholes in Israel suggests a cool temperate environment in the Pliocene, proceeding to alternating wet and dry climate states through the Pleistocene (Horowitz, 1989). Speleothems from the Negev Desert of Israel extending to Pliocene age were more rapidly deposited at ~3.1 Ma, indicating wetter conditions (Vaks et al., 2013).

During "Green Sahara" periods (GSPs), the Saharan desert climate was replaced by a savannah-type with greater precipitation. Anoxic conditions in the Mediterranean basin caused by enhanced freshwater runoff and fluvial organic matter may explain occurrences of sapropels (organic-rich sediments) found in marine sediment cores, so sapropels there seem to record occurrences of GSPs (Larrasoaña et al., 2013; Grant et al., 2022). Records from marine and lake cores suggest that GSPs lasted 4–8 ky at their most intense stages and have occurred repeatedly since at least 8 Ma or Late Miocene (Larrasoaña et al., 2013). Sapropels were somewhat less frequent after the Mid-Pleistocene Transition, though otherwise occurred with similar frequency before then (Larrasoaña et al., 2013). However, Grant et al. (2022) showed that Ti/Al ratios of sampled sediment cores recovered from the eastern Mediterranean were systematically lower in the early Pliocene and have risen since then. If their interpretation is correct, this also implies a wetter regional climate in the Pliocene. Alternatively, the change may have occurred because of a major change in the source of the Nile waters (Álvarez, 2023).

A study of the Mid-Pliocene warm period (3.3–3.0 Ma) by Li et al. (2018) included results of two atmosphere-ocean general circulation models, which suggested weaker northwesterlies by <1.0 m/s in both summer and winter. These imply that the winds flowing along the Red

Sea were modestly smaller, e.g., compared with ~5–12 m/s monthly mean winds for July and January 2009 in the Jiang et al. (2009) model. Modestly weaker winds in general are also suggested by global studies. Westerly zonal winds are expected to have been somewhat more subdued than pre-industrial modern times over the latitudes of the Red Sea by ~1–2 m/s, depending on the simulation (Li et al., 2015). Dust accumulation in deep-ocean cores and reconstructed ocean productivity also suggest that westerlies were weaker and lay more polewards (Abell et al., 2021). There is further evidence of smaller latitudinal temperature gradients globally in the Pliocene; Brierley et al. (2009) suggested there was only a ~ 2 °C temperature difference between the equator and 32°N in the Pacific at 4 Ma compared with ~8 °C today. Their result implies a weaker Hadley circulation than today, perhaps by 30%. Similar reduced temperature gradients were reported for the Atlantic and Indian oceans.

3. Materials and methods

3.1. Mass accumulation rates (MARs) at DSDP sites

To estimate MARs, dry bulk densities (DBDs) were taken from the laboratory-derived porosity and grain density data of Manheim (1974). Bulk carbonate contents (Fig. 2) were measured by Bode (1974a) but at different sediment depths to the Manheim (1974) measurements. We therefore estimated DBDs by interpolating between the DBD data to the depths of the carbonate measurements. Linear Sedimentation Rates (LSRs) were derived from the age models shown in Fig. 2 by linear interpolation, also to the depths of the carbonate data. The GeoMapApp-derived age models were used for this, except for the green line in Fig. 5 for which the Hughes and Varol (2024) model was used. MARs were then derived by multiplying the DBDs by the carbonate or non-carbonate fraction as appropriate and by the LSRs. These MARs were resampled every 10 ky. Because density and carbonate contents are likely under-sampled and because the age constraints are variedly spaced though roughly every 1-m.y., the MARs were averaged every 1 m.y. (Fig. 5). The text below only considers general variations, so this coarse temporal spacing is adequate.

3.2. Seismic reflection data

Seismic reflection data from deep-water areas were examined. Of those data studied previously (Mitchell et al., 2017; Mitchell et al., 2019; Mitchell et al., 2022), many have low resolution or poor signal/noise characteristics that prevent studies of the PP stratigraphy in detail. Some published shallow-seismic reflection data revealed some PP stratigraphy but no obvious mound-like structures (Bonatti et al., 1981; Bonatti et al., 1984; Guennoc et al., 1988; Richter et al., 1991; Ehrhardt et al., 2005; Ehrhardt and Hübscher, 2015; Feldens et al., 2016). The main datasets studied here are as follows.

The 3D seismic reflection data studied here were originally acquired offshore Egypt (Fig. 1) for BG plc in 1999 (Gordon et al., 2010). Details of the acquisition and processing parameters are not available, although the upward-curved reflections in the lower parts of the data suggest that they have been migrated. A total of 4879 cross-lines (SW-NE) were collected spaced 12.5 m apart and 1729 in-lines (SE-NW) spaced 25 m apart. Higher frequencies and hence better resolution can be observed towards the upper parts of these data. These data were interpreted using the software IHS Kingdom®. We show the topography of one surface within the PP, a cross-line profile and sediment thickness map derived from these data in Fig. 6. Some further surfaces and profiles through the seismic data volume have been published elsewhere (Ligi et al., 2018; Ligi et al., 2019; Mitchell et al., 2019; Ali et al., 2022; Ali et al., 2023).

The single-channel data in Fig. 7a were acquired in 1984 on RV *Conrad* during cruise RC2507 and recorded onto paper only (Martinez and Cochran, 1988; Cochran et al., 1991). Most of the data were collected with a water gun source, although airgun sources were occasionally used in the survey as well. Positioning by Loran-C was available
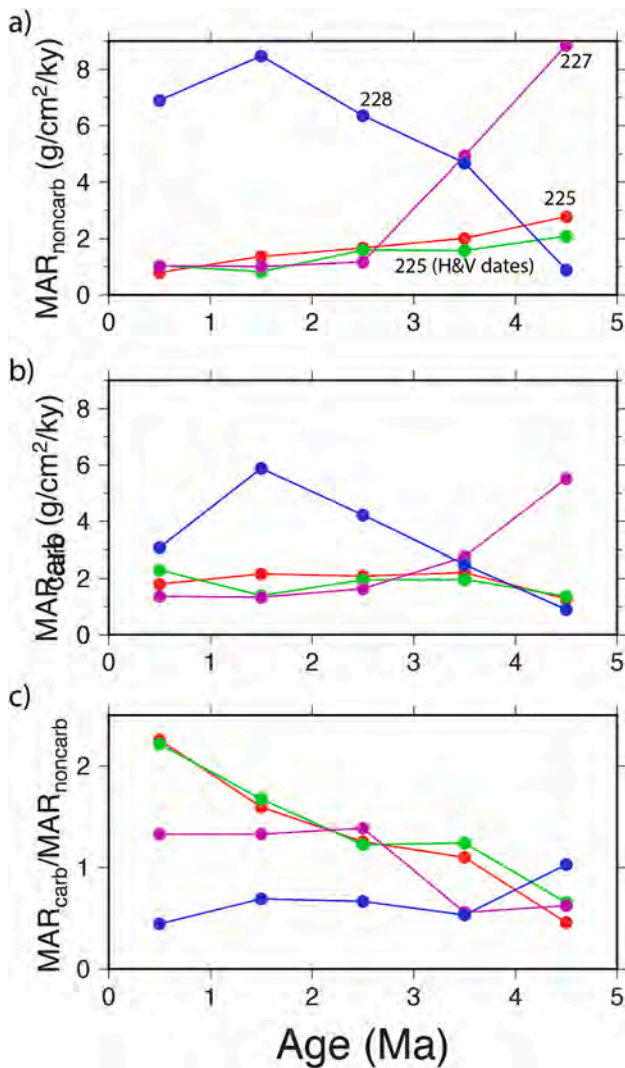
Fig. 5. Mass accumulation rates (MAR) of the (a) non-carbonate fraction and (b) carbonate fractions of the DSDP cores and (c) their ratio. Values were derived from laboratory-derived porosity and grain density data (Manheim et al., 1974) and bulk carbonate contents (Bode, 1974a), along with age models from GeoMapApp and (green line) Hughes and Varol (2024). For details, please see main text. (For interpretation of the references to colour in this figure legend, the reader is referred to the web version of this article.)

from the Saudi Arabian coast for 73% of the time, otherwise positioning was by transit satellite navigation and dead reckoning (based on data on ship speed through water and heading).

The data shown in Fig. 7b were acquired on RV *Urania* during cruise RS05 (Mitchell et al., 2010; Ligi et al., 2011; Ligi et al., 2012) with a Teledyne 48-channel streamer with 12.5 m group interval and two Sercel GI-Guns (airguns) for the source. These data have been processed to preserve amplitude ratios and the highest frequency contents to improve resolution of reflections within the PP. After predictive deconvolution, a time-varying prestack bandpass filter was applied with tapering from 12 to 16 and from 96 to 120 Hz (i.e., 16 and 96 Hz are the cut-off frequencies and 12 and 120 Hz mark the start and the end of tapering). Position data were acquired with the Global Positioning System (GPS).

Profile E (Fig. 7c) was acquired in 1979 on RRS *Discovery* with airguns and single-channel analogue streamer of unknown size (Searle, 1980). Navigation was by transit satellite and dead-reckoning between fixes. These noisy data were recorded onto paper only and are affected by a strong bubble pulse. Nevertheless, they show reflections to ~0.5 s

two-way time (TWT) beneath the seabed, including reflections within the upper Miocene evaporites.

The data shown in Figs. 7d and e were acquired with a Delta sparker source of Applied Acoustics with a short streamer on RV *Poseidon* in 2011 (Schmidt et al., 2011) and on RV *Pelagia* in 2018 (Augustin et al., 2019), respectively. Little information is available concerning the 2011 data acquisition. The 2018 data were acquired at ~3 knots with a 100-m multichannel streamer weighted to ensure a consistent towing depth of ~1 m. After bandpass filtering, normal moveout corrections were applied using a uniform 1500 m/s velocity and the resulting traces were stacked and time-migrated. Position data were acquired with the GPS.

The data shown in Figs. 7f, g and 9 were collected in 1965 during RV *Conrad* cruise rc0911 with a 25 cubic inch airgun and recorded onto paper only. Unfortunately, little further information is available on these data. Nevertheless, these data also contain reflections extending into the upper Miocene evaporites.

### 3.3. Seismic data interpretation considerations

The seismic lines of the images that we show do not intersect any of the DSDP sites, so direct ties of the seismic stratigraphy are not possible. However, a prominent reflection called the "S reflection" is widely observed in seismic data throughout most of the Red Sea (Phillips and Ross, 1970; Ross and Schlee, 1973; Mitchell et al., 2017; Mitchell et al., 2019). (Below we refer to the S-reflection as simply "S" for brevity.) Seismic travel time calculations (Whitmarsh et al., 1974) show that S in seismic data recorded over DSDP Sites 225 and 228 corresponds with the top of the Miocene evaporites, while at Site 227 it may correspond with a hard claystone that lies up to 32 m above the evaporites (hence still close to it). Interpreting this reflection allows us to identify the Plio-Pleistocene interval overlying S.

Interpreting stratigraphy in the lower PP can be complicated because (1) the lower PP away from coasts is commonly more transparent than the upper PP and (2) the PP sedimentary cover and substrate have likely moved variably since sediment deposition due to halokinetics (Mitchell et al., 2010; Augustin et al., 2016; Mitchell and Augustin, 2017; Mitchell et al., 2017; Mitchell et al., 2022; Ali et al., 2023) so stratigraphic surfaces may be strongly distorted compared with their geometries at the times when they were deposited at the seabed. For recognising contourites deposited in other open-ocean settings without these complications, Faugères et al. (1999) suggested the following characteristics: "major discontinuities that can be traced across the whole drift and represent time lines corresponding to hydrological events, lenticular, convex-upward depositional units with a variable geometry, and a specific style of progradation–aggradation of these units that is influenced by interaction of the bottom current with Coriolis force and with the morphology."

We have mitigated the effect of more muted reflectivity by selecting seismic data with higher frequency content or, in the case of the *Urania* data, boosting higher frequencies of digitally recorded data. The effects of halokinetic tectonic distortions are considered by using S as a reference surface. As younger PP sediments show tectonic growth structures and as deposition of typically denser sediments around halite beds tends to drive halokinetics (Gemmer et al., 2004), S was likely more nearly horizontal at the time of the Miocene-Pliocene boundary, like modern "salt flats" (Mitchell et al., 2017; Mitchell et al., 2021; Mitchell et al., 2022). Above diapirs, we observe occasional erosional truncations of underlying reflections (Mitchell et al., 2021; Mitchell et al., 2022; Delaunay et al., 2023) (and observations and interpretation below). Consequently, depressions of S have likely deepened relative to diapir crests since the early Pliocene.

We digitally flattened three sections of seismic data at S (flattening is a process in which seismic traces are offset vertically so that a reference reflection occurs at a common vertical position along the section; Figs. 6c, 7d and e). As an example, the yellow line in Fig. 6b shows the two-way times used in flattening that section. If the surface forming S
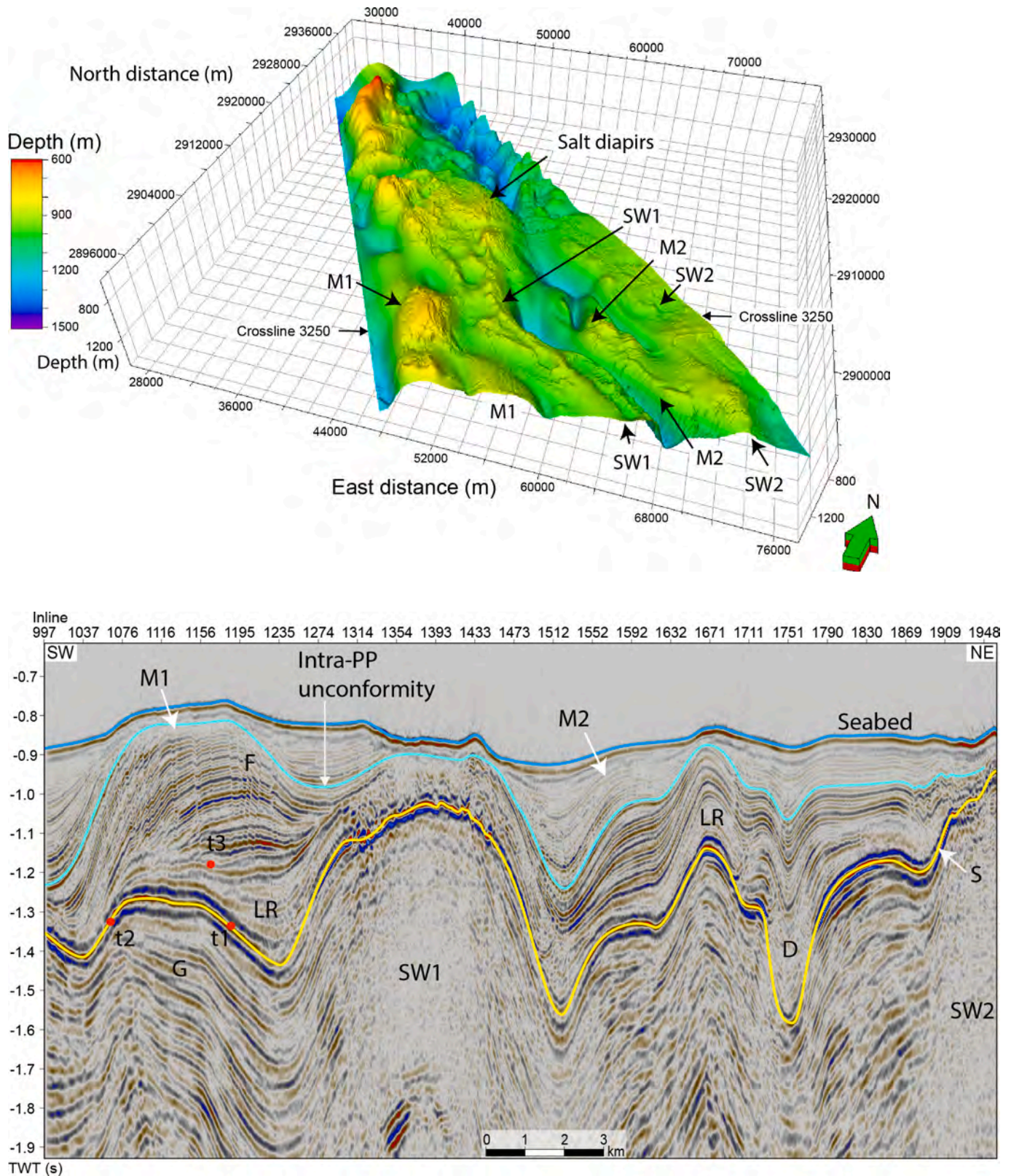
Fig. 6. Images derived from a part of an industry 3D seismic polygon (Gordon et al., 2010) selected as showing contourite-like reflection geometries. Extent of selected data is shown by red-filled polygon in Fig. 1. (a) Three-dimensional view of a reflection within the deposits (located by blue line in (b)). Coordinates are in Universal Transverse Mercator (zone 36). (b) Cross-line 3250 (located in (d)) marked with the interpreted S-reflection (yellow), chosen internal reflection with unconformity (turquiose) and seabed (blue). Annotations: M1 and M2, sedimentary mounds, SW1 and SW2, salt walls, D, depocentre, F, fault, LR, low reflectivity, G, tectonic growth stratigraphy, S, S-reflection, TWT, seismic two-way time, t1-t3, PP reflection terminations. (c) As (b), with traces offset vertically so that the S-reflection appears at a common two-way time. (d) Map of thickness of deposits between the S-reflection and the interpreted unconformity (yellow and turquoise lines in (b)). Annotation as (b). (For interpretation of the references to colour in this figure legend, the reader is referred to the web version of this article.)
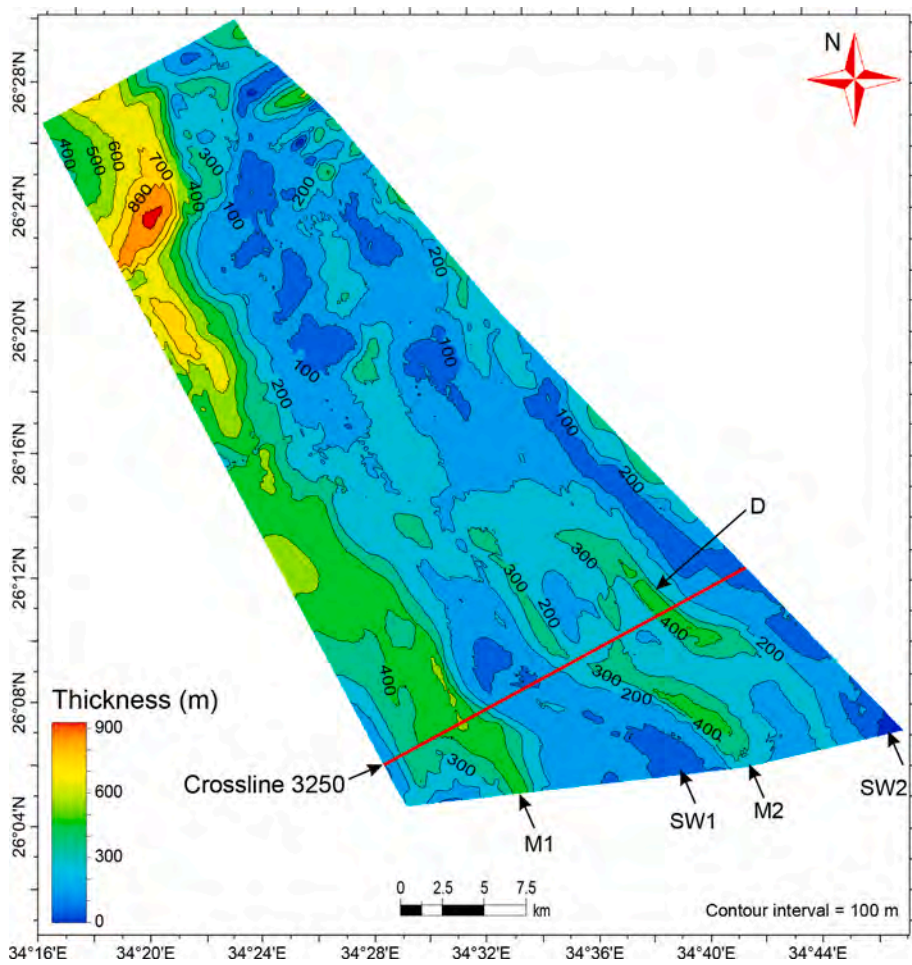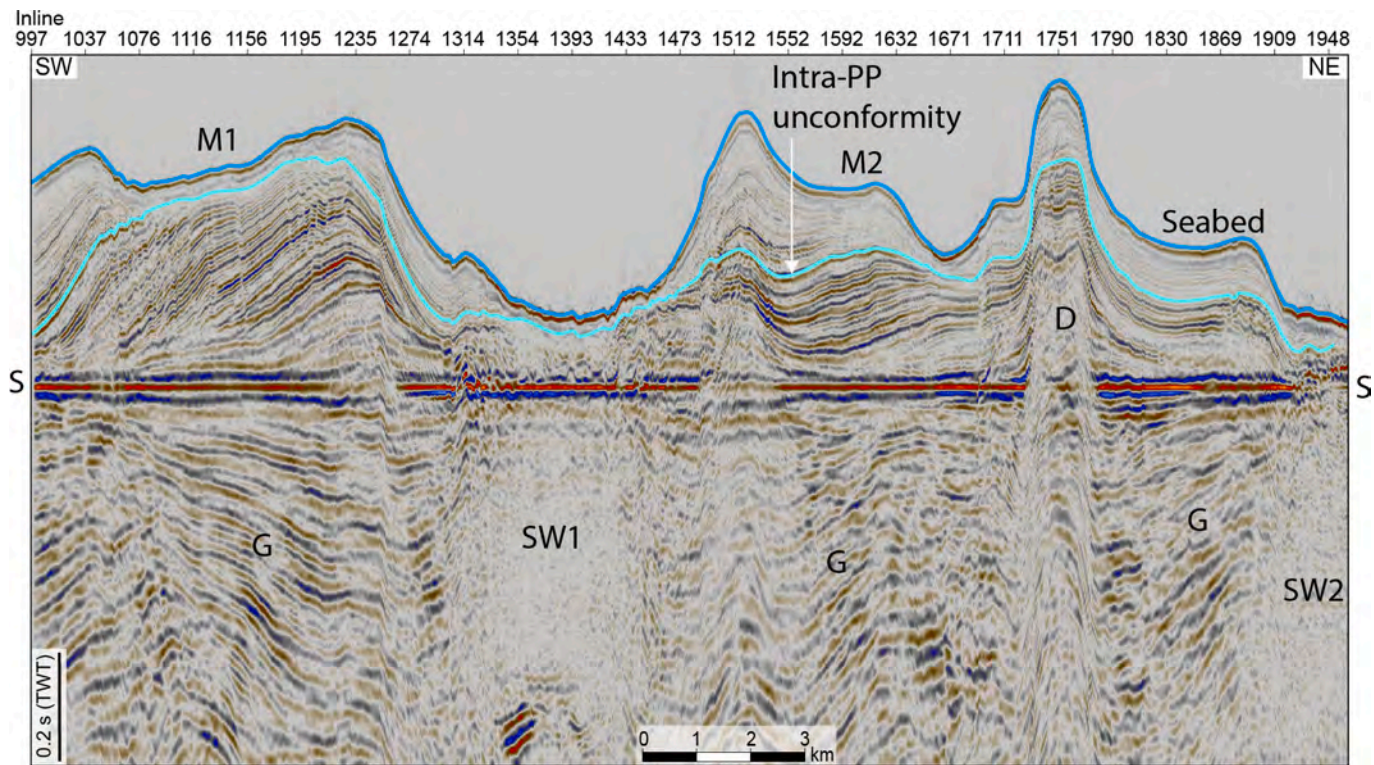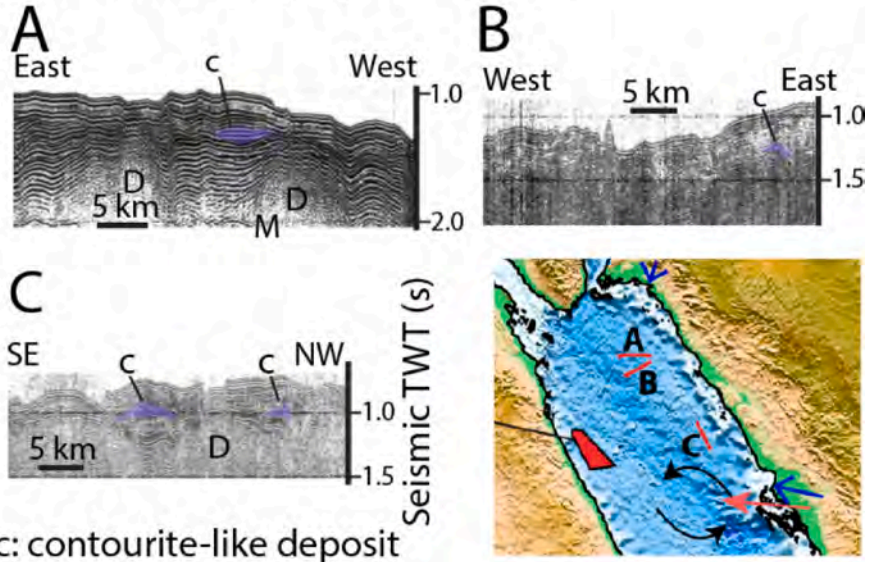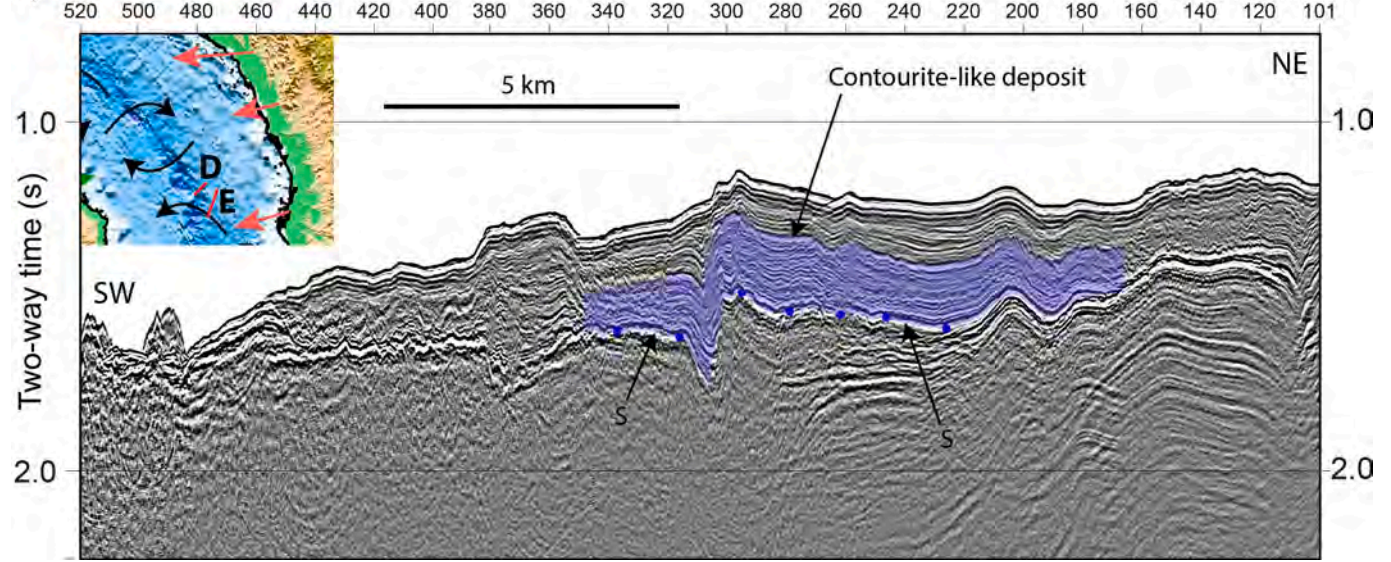
Fig. 6. (*continued*).
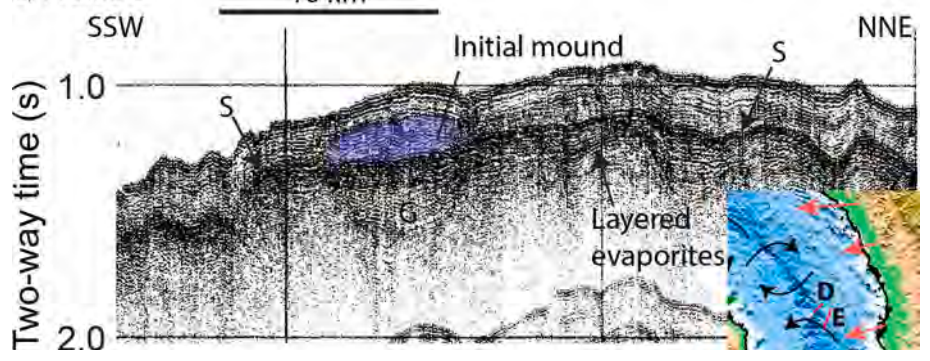
Fig. 7. Examples of sediment mounds in seismic reflection data (profiles A-I are located in Fig. 1a, partial copies of which are inset within panels). Annotation includes: C: contourite-like deposits, S: S-reflection marking top of Miocene evaporites, D: salt diapir, E: layered evaporites. Vertical axes show seismic two-way travel time in seconds. The contourite-like deposits are highlighted with blue polygons. (Their tops are at arbitrarily chosen reflections, in some cases within the overlying pelagic sequence, in practice morphology tends to grade upwards and is not discrete. Image quality dictates extent of interpretation, hency polygons do not represent total extents). Where shown, blue-filled circles mark the S-reflection).
(a) Compilation of data collected with a watergun source during cruise RC2507 (Cochran et al., 1991) obtained from https://www.ncei.noaa.gov.

(b) Airgun seismic data collected in the central Red Sea in 2005 (Ligi et al., 2011; Ligi et al., 2012).

(c) Airgun seismic data collected in 1979 (Searle, 1980).

(d) Sparker seismic data collected near Jeddah on RV Poseidon in 2011 (Schmidt et al., 2011). Lower panel shows the section flattened by offsetting traces to a common two-way time of the S-reflection. T: vertical transition in reflection geometries.

(e) Sparker seismic data collected offshore Sudan on RV Pelagia in 2018 (Augustin et al., 2019). Red dots and annotation t1 and t2 locate examples of PP reflector terminations at S (lines indicate the reflections concerned). Lower panel shows flattened section, as in (c).

(f) and (g) Airgun seismic data collected during RV Conrad cruise RC0911.

(For interpretation of the references to colour in this figure legend, the reader is referred to the web version of this article.)
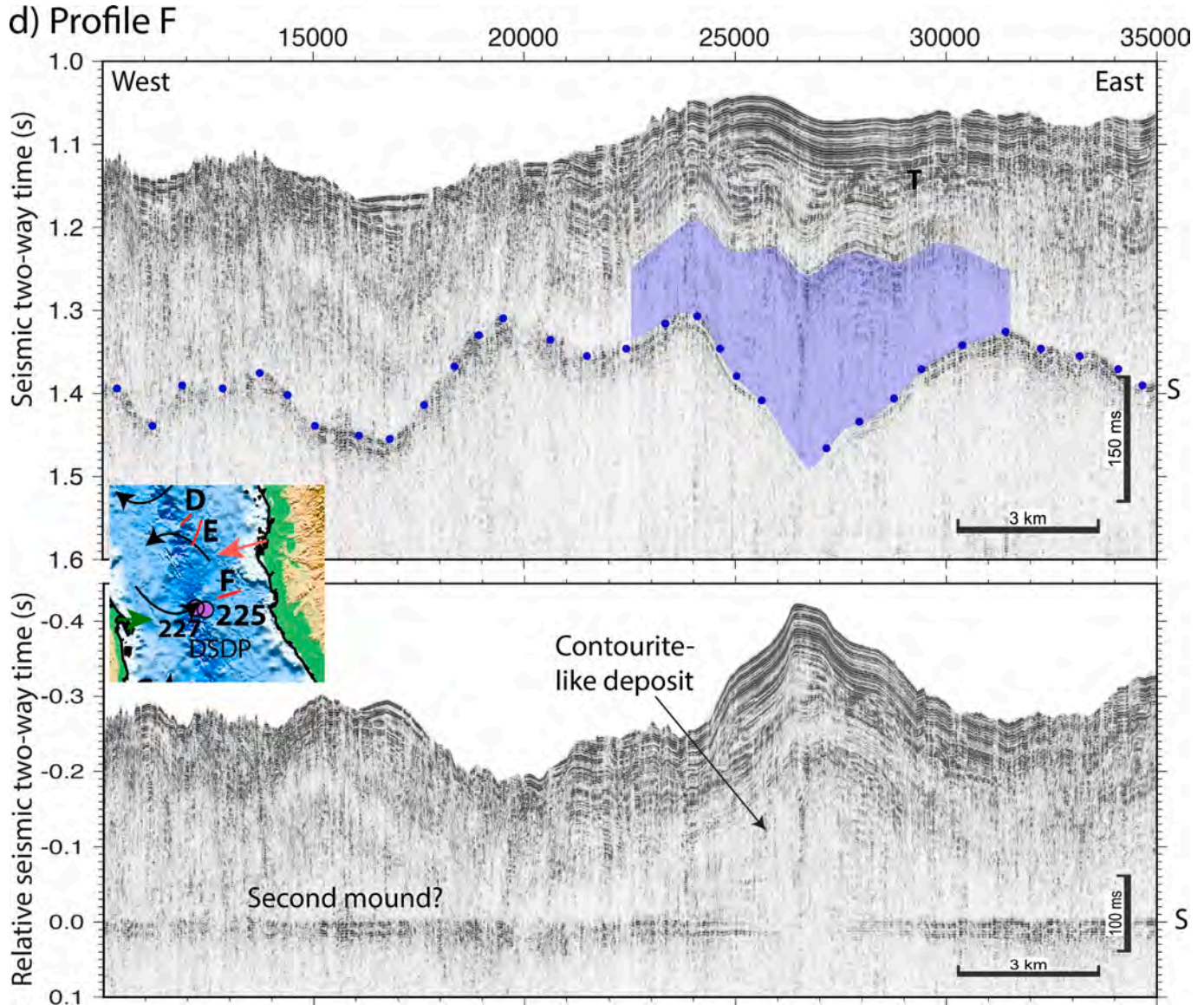

Fig. 7. (*continued*).

were perfectly flat at the start of the Pliocene and the sediments have been deformed only gradually by halokinetic deformation and only weakly by compaction, the lower PP reflections in these flattened sections should better approximate their original depositional geometries. As halokinetic deformation has also occurred progressively in many places after the end of the Miocene, the upper PP in these flattened sections is likely over-compensated for the deformation. Nevertheless, these flattened sections are helpful for interpretation if we bear these complications in mind.

Although the older seismic data originally recorded on paper are generally of lower quality, they nevertheless reveal a prominent S. In these data, guided by our experiences with the digital data, we sought reflection packages within the PP that are discordant with S, i.e., they have different dips and would form mounds if S were flattened out. Spatially uniform (pelagic) accumulation of sediments over a mound can be expected to lead the geometry of the mound to continue higher up in the stratigraphy, hence we interpret mounds where this geometry is found over some harder-to-interpret transparent lower PP (e.g., Figs. 7f, g). Conversely, reflections that merely parallel S suggest more pelagic-like deposition. These are not as satisfactory as the higher-quality digital examples, though we include them as they suggest broader occurrences of these mounds.
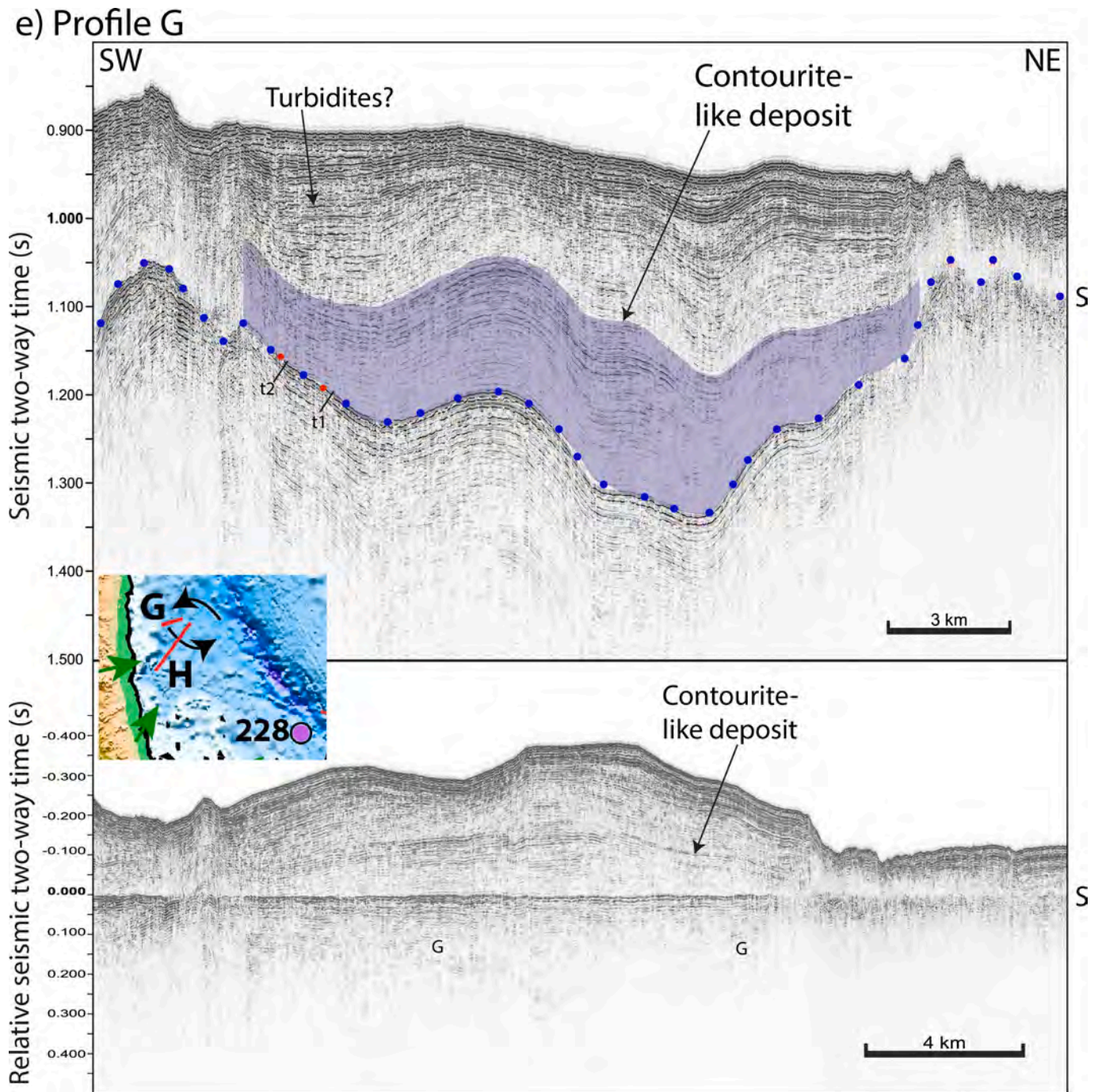
Fig. 7. (*continued*).

4. Observations

4.1. Mass accumulation rates (MARs) at DSDP sites

The estimated carbonate and non-carbonate MARs show long-term trends in deposition at the sites (Fig. 5). The effect of possible date uncertainty is suggested by differences between the curves derived using the revised dates within www.geomapapp.org and those provided by Hughes and Varol (2024); MARs differ by about a quarter in places. For sites 227 and 228, some variations in MAR occurred in both carbonate and non-carbonate components; for Site 227 from 5 to 2 Ma and for Site 228 from 5 to 1 Ma. However, for Site 225, carbonate MARs are nearly flat for 0–4 Ma on average using either of the two biostratigraphic

schemes, whereas the non-carbonate MARs declined from 2.01 g/cm^2/ky (3–4 Ma) to 0.79 g/cm^2/ky (0–1 Ma).

4.2. Seismic reflection data

The profile in Fig. 6b through the southerly part of the 3D seismic volume reveals a prominent S with ~0.5 s TWT of relief. Over the top of salt wall SW1, S is more irregular in character and rugged. As observed elsewhere in the Red Sea (Mitchell et al., 2015), some parts of the stratigraphy immediately above S have low reflectivity ("LR" in Fig. 6b). Below S, besides within the two salt walls, the section is reflective. In places, reflections below S increase in dip downwards (e.g., at "G" in Fig. 6b).
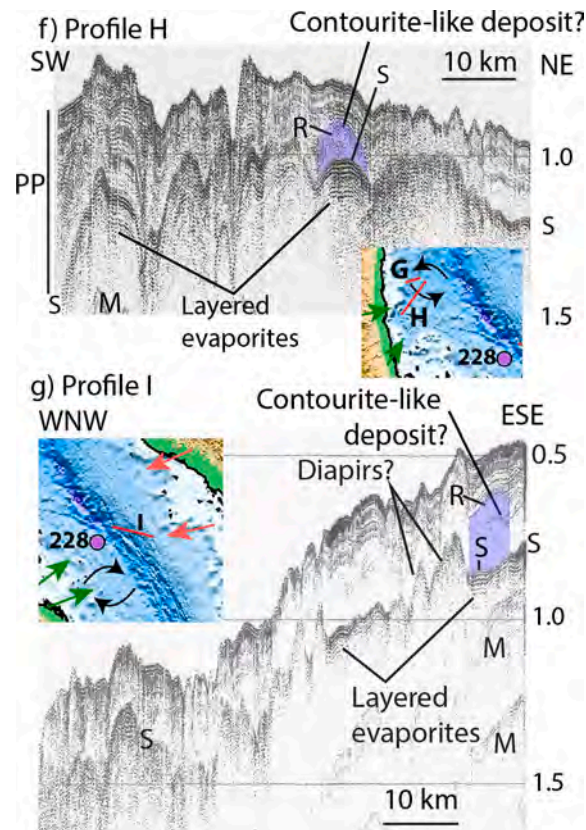
Fig. 7. (*continued*).

Overlying S in Fig. 6b, reflections from within the PP (overlying S) vary in geometry and only partly follow the topography of S. Centred on in-line 1156, the reflections form a mound-like sigmoidal body marked "M1", offset to the SW from SW1. At in-line 1235, the PP reflections immediately above S are locally more widely spaced. A further sigmoidal body occurs at in-line 1592 ("M2"). Near in-line 1751 where marked "D", the reflections are poorly recorded, though reflections higher in the PP can be observed and have smaller relief than S below them. Some offsets of reflections can be observed above S though not affecting it ("F" in Fig. 6b).

Some truncated reflections within the PP suggest the presence of unconformities. The topography of the unconformity marked in turquoise in Fig. 6b is shown in three-dimensions in Fig. 6a. The unconformity surface, and hence much of the central and lower PP, is elongated in a series of irregular ridges oriented NW-SE. This elongated character is also shown by the map of thickness of sediment between that reflection and S (Fig. 6d), with M1 thickening to >800 m thickness in the north. Its thickness is less irregular going to the north than the topography in Fig. 6a.

Under M1, truncations of PP reflections in the earliest sediments (marked "t1" in Fig. 6b) lie close to the depression of S under in-line 1235. Terminations of reflections of subsequent deposits are further SW (t2). Above the reflections marked LR, terminations again lie near the depressions (t3). Terminations of reflections from younger deposits lie progressively to the SW.

In the flattened section (Fig. 6c), S has a relatively uniform character along the profile except over the salt walls and under "D". In three areas marked "G", dipping reflections below S steepen with depth. Above S, the lowermost PP is anomalously thick at in-line 1235 and 1671. Above and southwest of those positions, the mound-like deposits M1 and M2 contain sigmoidal clinoform-like sequences of reflections dipping to the southwest.

The RC2507 images (Fig. 7a) commonly do not show a prominent S,

presumably due to the high seismic frequencies associated with the watergun source and layered terrigenous sediments in the northern Red Sea, which also produce prominent reflections. However, one profile (not shown) crossed the 3D seismic volume, where S is clear, so we were able to confirm our identification of S there. A number of lensoid deposits can be observed in profiles A-C, where they are 100 ms or more TWT in vertical extent and extend a few km along the profiles.

In profile D, a reflection at the upper edge of the blue polygon shown in Fig. 7b has a varied vertical separation from S below it. The sediment body encompassed by the upper reflection and S is thickest where marked "contourite-like deposit" and thins progressively away from that location to both NE and SW. Interpretation is difficult SW of shot point (SP) 360, hence the blue interpretational polygon stops there, but the deposit appears to be also thick at SP 360–380 and thins out towards SP 480 where S rises towards the seabed. If the topography of S developed progressively, this sediment body would have been a modest mound of 100–200 ms relief (~100–200 m) and > 10 km extent when it was deposited. An irregular step of S from SP 325 to 300 coincides with the edge of a salt flow mapped with multibeam sonar data (Mitchell et al., 2010); data NE of there lie over the more mobile flow.

In profile E, S is marked by extended reflectivity. It generally dips gently to the SSW along the southerly half of the profile and is underlain by reflections varying in dip ("G" in Fig. 7c). Overlying S, the upper half of the PP contains reflections that mimic the seabed. Where highlighted in blue in Fig. 7c, these reflections form an upward-convex rounded geometry that it is different from the more gently dipping S. Towards the base of the blue highlighted area, reflections are oriented similar to the modern seabed ("Initial mound") and also diverge from S.

In profile F (Fig. 7d, top panel), S is prominent and has a different dip from the reflections above it. The upper limit of the dipping reflections within the lower PP ends abruptly at "T" marked in Fig. 7d. Above "T", the reflections are flatter. Profile F illustrates the lower reflectivity of the lower PP compared with the prominent S and the reflective upper PP. S

in these data comprises two prominent wavelets spaced vertically ~10–20 ms, which can be traced almost 20 km distance. In the flattened section (Fig. 7d, lower panel), S has a uniform character and the two wavelets maintain their spacing across the profile. The mound reaches ~200 ms in vertical relief and is ~10 km across. Unlike that in profile D, here the mound has a sharper peak thickness coinciding with the valley in S observed in the top panel. A possible second mound occurs at SP15000.

Within profile G, PP reflections are difficult to trace across the whole line, although one horizon has been approximately located by the upper surface of the blue polygon in Fig. 7e. The interval between that horizon and the prominent S varies along the profile, though it is roughly lensoid and thickest about half-way along the image. The profile further illustrates the weaker reflectivity of the lower PP, though still strong S. S is laterally continuous in character across much of the section. Reflections beneath S are not all parallel to S but tend to dip downwards towards the centre of the contourite-like deposit and steepen with depth. Reflection terminations against S within the lower PP are hard to identify, though appear to lie further from the centre of the blue polygon for sediment deposited later (hence "t2" lies SW of "t1" in Fig. 7e). In the flattened section, S has a somewhat uniform character along the profile. On the left side of that profile, reflections beneath S dip modestly downwards to the NE with increasing dip with depth ("G" annotation). On the right side of the profile, though less clear, similar reflections (also marked G) dip to the SW. Both sets dip towards about the centre of the area where S is depressed.

Profiles H and I contain prominent S and in places strong layering below S ("layered evaporites" in Figs. 7f and g). In the PP above S, the data are variably layered, though with the lower PP generally less reflective. The PP typically drapes the underlying S, a sign of pelagic-like accumulation of particles. However, in profile H where marked "contourite-like deposit?", reflections dip to the SW within the left side of the blue polygon and to the NE on the right side (marked "R"). These contrast with S which is almost flat for 1–2 km beneath it, i.e., these two sets of reflections diverge. In profile I, where also marked "contourite-like deposit?", a series of reflections ("R") can be observed that also diverge from the underlying S.

5. Interpretations

5.1. Mass accumulation rates at DSDP sites

Multibeam data show that DSDP Sites 225 and 227 both lie on a salt flow (Augustin et al., 2019), so the PP sediments on top of the Miocene evaporites have moved further from the coast of Arabia since they were deposited. An evaluation of geophysical data suggests that they moved seawards by >25 km and perhaps by as much as 50 km (Supporting Information). This helps to explain their high non-carbonate MARs early in the Pliocene and the subsequent decline in those MARs (Fig. 5a). The multibeam data and drilling report (Whitmarsh et al., 1974) show that Site 227 lies close to an axial deep. The carbonate and non-carbonate MARs varying similarly from initial high values at 4–5 Ma might be due to downslope transport and preferential accumulation of sediment at Site 227. As Site 228 is thought to have been influenced by sediment dispersal from the Tokar Delta (Whitmarsh et al., 1974), the increasing non-carbonate MARs for that site from 4 to 5 towards 1–2 Ma may also have a transport origin. Increasing biological activity associated with the delta and towards the southern Red Sea (Bouilloux et al., 2013) also complicate interpretation of carbonate MARs for Site 228.

However, for Site 225, the nearly flat carbonate MARs from 4 to 0 Ma, occurring while the non-carbonate MARs declined, may have a different origin. We interpret the increasing percentage of carbonate up-stratigraphy (Fig. 2a) as mainly a dilution effect of the decreasing rate of deposition of non-carbonate material (Fig. 5a) rather than increasing rate of carbonate deposition. Potentially confusing this interpretation, the carbonate component of these cores may partly originate from

erosion of carbonate rocks on land (terrigenous). However, petrographic study by Stoffers and Ross (1974) revealed no evidence for terrigenous carbonates, except for some dolomite (2–20%), much of which could be authigenic. They interpreted the sediment as largely pelagic carbonate ooze and chalk. The MAR data therefore imply relatively constant productivity of pelagic organisms throughout the PP after 4 Ma or at least do not reveal any major change. However, the lower carbonate MAR for the 4–5 Ma interval suggests a lower productivity in the early Pliocene. Lower initial carbonate MAR is suggested using both sets of dates and, in the case of the Hughes and Varol (2024) set, constrained by dates either side of this age range (Fig. 2). We suggest that Site 225 best represents the history of deep water conditions of the Red Sea, which therefore experienced a relatively constant rate of carbonate deposition after 4 Ma.

5.2. Seismic reflection data

We first address the character and geometry of S and reflections below it, as their interpretation affects how the overlying PP reflections are interpreted. Where S is irregular over salt walls and diapirs, in places accompanied by truncated underlying reflections, we interpret the surface forming this reflection as having been eroded, perhaps during a widespread event in which the Red Sea drew down, exposing parts of the Miocene evaporites to waves and/or rainwater (Coleman, 1974; Colombo et al., 2014; Mitchell et al., 2017). In contrast, the lack of an unconformity at S away from such areas suggests that the surface creating that reflection was deeper and not exposed to waves or rainfall (Mitchell et al., 2022), e.g., these areas may have been covered by water or brine at that time. A nearly flat-lying or uniform environment of evaporite deposition is suggested where reflections at S and immediately below it are relatively uniform in character and spacing across the section, such as in Figs. 6c, 7d and e (flattened sections). In contrast, deep basins filled with gravity-flow deposits would appear very differently, with more angular terminations of overlying reflections with S. As explained earlier, the reflectivity below S likely corresponds with alternating halite, anhydrite and shale beds. The increasing dips with depth of these evaporite reflections, particularly revealed by the flattened sections in Figs. 6c and 7e, indicate tectonic growth stratigraphy. Subsidence therefore occurred during deposition of these strata, such as due to the greater density of anhydrite in them compared with halite dominating the diapirs (Mitchell et al., 2022). As the small faults in the data above S in Figs. 6b and c do not offset S, they likely originate from differential compaction and are not considered further.

In some areas of the flattened seismic sections, reflections from PP strata immediately overlying S are dipping and they steepen upwards away from S (e.g., around in-line 1200 in Fig. 6c and above the two "G" annotations in Fig. 7e). These may suggest that the halokinetic deformation continued into the Pliocene with a similar spatial pattern, e.g., if driven by the ongoing extensional tectonics. However, the uniform spacings of reflections around S in Figs. 6c and 7e suggest that, at the time that the late Miocene and earliest Pliocene sediments were deposited, the seabed did not form a local basin but was nearly flat there. The increasing thickness of sediments within the mounds, as they were deposited, can be expected to increase vertical stress within the underlying evaporites by amounts that are comparable with the activation stress of halite deformation (Rowan et al., 2019) so the mounds may have further promoted local subsidence (Mitchell et al., 2022). Deposition of these mounds varied in spatial extent from initially localised (t1 in Fig. 6b), then broad (t2), then narrow (t3) and subsequently broad again.

Where the deposits form mounds in the seismic images (Figs. 6b, 7a, b, c, f, g), there should be no debate over whether they formed mounds on the evaporite surface in the early PP. Based on the last two paragraphs and particularly the continuity of the S reflections, we interpret the lower PP deposits lying within depressions of S (Figs. 7d, e) as also likely to have formed mounds. This implies the presence of mounds

along many parts of the Red Sea at varied distances from both coasts (Fig. 1).

In the profiles other than F, the PP reflections within or above the polygons shown are either parallel to the seabed (profiles A, D) or somewhat discordant with the seabed (e.g., profiles B, G, I). Besides some local areas of flat-lying deposits likely to be gravity flow deposits (e.g., profile G), in general, the reflections within these bodies vary gradually in dip towards the modern seabed, suggesting a gradual change in the currents or in the grain size of particles influencing their transport and deposition. The unconformity marked in Fig. 6b suggests that bottom conditions varied abruptly locally there, although otherwise that image also contains gradually varying dips of reflections.

In contrast, an abrupt transition in reflection dips is observed in profile F ("T" in Fig. 7d). Profile F was collected over a major collapse structure, where the evaporites have flowed into the spreading centre (Augustin et al., 2014; Feldens and Mitchell, 2015; Mitchell et al., 2021) (also see electronic supplement). As changes in oceanographic circulation are likely to have a more widespread influence and the change occurs only in profile F, it probably only has a local origin. We suggest that it is related to the collapse and hence not relevant to Red Sea circulation.

M1 lies on the SW side of a salt wall and resembles features that Faugères et al. (1999) described as plastered drifts. Its irregular topography (Fig. 6a) is likely due to varied halokinetic deformation, which has affected its thicknesses much less (Fig. 6d). Besides that irregularity, peaks in the surface of M1 lie at roughly similar elevations, as would be expected of a contourite. Its greater thickness in the north might indicate that sediment was mainly introduced from the north and has been variably dispersed to the SE by currents along M1. The other mounds resemble the mounded drifts of Faugères et al. (1999). Their geometries in plan-view are harder to determine. The mound in profile E may correspond with the mound in profile D, implying an elongate deposit between these lines oriented roughly NW-SE. In the multibeam sonar data, the step in S down to the SSW at the left-most "S" annotation in Fig. 7c is the northerly edge of a salt flow, hence terrain to the NNE of it is somewhat more stable. Another elongate mound might lie between profiles G and H, oriented roughly N-S, although those profiles are more widely separated.

We have not generally observed sediment waves or moats that can sometimes be associated with current-influenced pelagic deposition (Flood, 1988; Mitchell and Huthnance, 2013). (In Fig. 6b, the irregularities of reflections within M1 are more likely to be due to minor normal faults.) Moats should be resolvable in some of our higher resolution seismic data and their absence suggests that the formative currents were modest (Wilckens et al., 2023).

6. Discussion

The observations and earlier research suggest how the Red Sea has changed over the PP. At around the Miocene-Pliocene boundary, the Red Sea became fully isolated, creating an unconformity observed at the S-reflection in many deep-water parts of the basin (Izzeldin, 1987; Mitchell et al., 2015; Mitchell et al., 2017; Mitchell et al., 2021; Delaunay et al., 2023). Mitchell et al. (2022) showed a map of the unconformity for the central Red Sea, occurring intermittently between both Nubian and Arabian coasts. This event was followed by flooding and development of the circulation, creating the mounds described here. The circulation started near the beginning of the Pliocene when the central Red Sea flanks were much shallower, ~192 m deep on average (70–387 m range given reconstruction uncertainties (Mitchell et al., 2021)). The basin was also ~60 km on average narrower in the earliest Pliocene because of plate-tectonics based on an average spreading rate of 12 km/m.y. (Chu and Gordon, 1998). From the combination of shallower depths and narrower basin, the water body would have been at least five times smaller in volume. The rainfall catchment, however, was not so greatly affected. We estimate that it would have been only

11% smaller in the earliest Pliocene due to plate tectonic motions (60 km × 1800 km = 10^5 km^2 change compared with 10^6 km^2 total catchment (Fig. 1)). The drainage divides of the early Pliocene were likely located not much differently from the modern ones, as escarpments and other relief around the Red Sea have mostly developed (Steckler and Omar, 1994; Boone et al., 2021; Turab et al., 2023) since the main rift-shoulder uplift and synrift sediment deposition at ~20 Ma of rifting (Bosworth et al., 2005; Bosworth, 2015), much older than the 5.3 m.y. of the PP.

The early Pliocene (Fig. 3) or uppermost Miocene (Caruso et al., 2013) $\delta^{18}O$ values reaching −5‰, therefore, seem plausibly explained by the smaller Red Sea being more susceptible to dilution by rainwater, given also evidence of a wetter climate (Vaks et al., 2013; Liddy et al., 2016). If we use the $\delta^{18}O$ values of speleothems from the Pliocene Levant (−11‰ to −10‰ (Vaks et al., 2013)) to represent rainwater, we can speculate on the dilution caused by simple mixing with waters with 0‰ $\delta^{18}O$ originating from the Indian Ocean (roughly, as in practice rainwater $\delta^{18}O$ varies by several ‰ in continental interiors (Tian et al., 2018)). The −5‰ to −4‰ $\delta^{18}O$ of Fig. 3 and Caruso et al. (2013) then imply that the normal 35‰ salinity of seawater was reduced to 13–18‰. These are below the ranges of salinity tolerated by *G. sacculifer*, *G. ruber*, and *G. siphonifera* (Fenton et al., 2000), thus potentially explaining their absence in the early Pliocene samples (Fig. 4). Furthermore, the growth of dolomite has been recently shown to be promoted by cyclical under- and over-saturation for the mineral (Kim et al., 2023). Dolomite is common in the lowermost unit 3 immediately above the Miocene evaporites (Stoffers and Ross, 1974; Supko et al., 1974). Its presence may be explained by cycles of freshening by rainwater. Because there are no abrupt changes in the stratigraphy besides in profile F and locally at the unconformity in Fig. 6b, the circulation that produced these sedimentary mounds near the seabed reduced over the PP gradually.

Comparing the locations of the mounds to the locations of wind jets (Fig. 1), and as wind directions are varied, aeolian sediment input is likely to have been too dispersed to have created the mounds. Fluvial input is also likely to lead to broader input of terrigenous sediment than the limited lateral extents of the mounds because of surface currents and because mound locations do not obviously correspond with drainage outlets. We therefore suggest that the mounds formed by physical movements of sediments within the sea and consider the following two processes plausible:

6.1. Thermohaline circulation

Some of the paleo-environmental indicators outlined earlier support a thermohaline circulation, perhaps involving a greater water exchange with the global oceans by the mid-PP. For example, the low variability of $\delta^{18}O$ values in the mid-PP suggests a lack of intermittent evaporative concentration of ^{18}O (Fig. 3) that occurred in the Late Pleistocene. Such low variability would occur if waters were replenishing rapidly. The lack of hard layers in the DSDP cores (Fig. 2) and lack of reflectivity in seismic data of the lower PP suggest that the basin did not become sufficiently saline to precipitate inorganic aragonite. The marginal marine deposits of the Pliocene Ifal Group of Arabia also do not apparently contain cement-rich layers (Hughes and Johnson, 2005).

Modelling by Thran et al. (2018) suggested that the mean bottom current speed over contourites in the global ocean is 2.2 cm/s. If RSDW production rates in the Pliocene northern Red Sea were comparable with 1.6×10^5 m^3/s modern rates (Cember, 1988) and considering the narrower basin at the time, the water movement would need to have occurred in a body of ~100 m vertical thickness in order to produce a mean current of 2.2 cm/s. As the Red Sea sediments are coarser than deep-ocean silts (Fig. 2), the presence of contourites could imply a larger current speed and hence a vertically smaller water body, if this explanation is correct.

Could a thermohaline circulation have been caused by production of RSDW in the Gulfs of Suez and Aqaba and shelves around the

northernmost Red Sea, like in the present day? We have only limited knowledge of the past physiography, but platform carbonates and other shallow-marine Plio-Pleistocene deposits have been identified around the coasts, such as in the Midyan region (Fig. 1) of NW Arabia (Hughes et al., 1992; Hughes and Johnson, 2005; Angeletti et al., 2019; Taviani et al., 2019). The PP has been studied in a number of wells immediately to the SE of the Gulf of Suez (Hughes et al., 1992; Hughes and Johnson, 2005; Faris et al., 2023). Hughes and Johnson (2005) noted the presence of moderately deep-water foraminifera in the Pliocene Warden Formation of the outer Gulf of Suez. As "very deep-marine" assemblages are considered to occur in depths >200 m (Hughes et al., 1992), a "moderately deep environment" may not necessarily be excessive from the point of view of deep-water production (<100 m?). Tawfik and Krebs (1994) inferred shallow-marine to brackish environments from Pliocene diatoms there. In contrast, Pocknall et al. (1999) inferred at least four marine incursions into the northern Gulf of Suez during the Pliocene, with mostly marine conditions indicated by diatoms recovered at a well in the central part of the gulf.

Importantly, PP gypsum deposits have been reported along the Red Sea coast, where they were deposited in lagoons behind coral reefs, and within the Gulf of Suez (Orszag-Sperber et al., 1998a; Plaziat et al., 1998; Pocknall et al., 1999; Taviani et al., 2019). According to experiments of Briggs (1958), Gypsum starts to be deposited from evaporating seawater when it reaches a density of 1.13 g/cm^3. Although the density of any outflow from gypsum-producing areas would have been reduced by dilution, 1.13 g/cm^3 is ~10% larger than normal ocean water of 1.025 g/cm^3. If the Red Sea was brackish overall (Caruso et al., 2013), the contrast may have been larger. RSDW locally produced around the northern Red Sea therefore potentially had greater negative buoyancy than today, implying a more vigorous flow from these marginal basins that may explain particularly the northern mounds such as M1 (Fig. 1).

The northwesterly winds acting on the surface of the Red Sea presently oppose the thermohaline circulation (Fig. 8a). The 10–20% weaker winds of the Mid-Pliocene warm period (Li et al., 2018) modestly reduced that opposition. The amounts may appear small but stresses in turbulent boundary layers increase with the square of the mean speed, so the models suggest surface stresses were reduced by ~20–40%. In the modern southern Red Sea, stratification prevents the loss of saline RSDW to the Gulf of Aden over Hanish Sill (Fig. 8a). That stratification also opposes rapid deep-water movement in the Red Sea. In contrast, if the

earlier PP sill between the Red Sea and Gulf of Aden were deeper (Fig. 8b, c) and the sea were generally shallower (Mitchell et al., 2021), this combination may have allowed the escape of RSDW into the Gulf of Aden and prevented extremes of salinity developing in the basin.

Knowledge of the past physiography of the Hanish Sill and Bab el Mandeb Strait through the PP is poor and our proposed earlier deep connection with the Gulf of Aden may seem to be contradicted by the general extensional tectonic environment of the region. However, GPS measurements show that there is negligible movement presently across the Bab el Mandeb Strait (McClusky et al., 2003; Reilinger et al., 2015; Viltres et al., 2020). On some islands within the strait, alignments of young cones suggestive of volcanic dykes are oriented perpendicular to the rift (Mitchell and Bosworth, 2024) not parallel to it as expected for volcanic rifts. Volcanic Perim Island at the entrance to the strait has been dated by K/Ar at 10.5 ± 1.0 Ma (Mallick et al., 1990). Hanish and Zukur islands (Fig. 1) contain only weakly eroded cinder cones, suggesting recent volcanism (Gass et al., 1973; Rogers, 1993). Therefore, volcanic structures may have been emplaced later in the PP, constricting the flow, but were absent in the earlier PP. Furthermore, the shallow banks around the channel, including near Hanish Sill, are productive carbonate factories (Einsele and Werner, 1972). Exported shallow-water particles have been interpreted from Pleistocene cores at DSDP Site 229 near those banks (Fig. 1) (Whitmarsh et al., 1974). One line of seismic data shows slope progradation into the southerly axial trough (Mitchell and Sofianos, 2019). Progressive growth of the banks and progradation of slopes around them may have constricted the channel gradually. Rohling et al. (2009) modelled variations in $\delta^{18}O$ in deep-water Red Sea sediments due to evaporation accounting for hydraulic exchange with the Gulf of Aden. Their model successfully reproduced the global sea-level curve of the last 500 ky when 0.02 m/ky uplift at Hanish Sill was included. If such uplift occurred before 500 ka at the same rate, the sill would have been deeper by 20 m at 1 Ma and by 100 m at 5 Ma. Given that the central Red Sea flanks were only ~192 m deep at the start of the Pliocene (Mitchell et al., 2021), the latter value implies that there would have been limited obstruction to outflow of RSDW into the Gulf of Aden at Hanish Sill (Figure ic).

Seismic reflection data around the Bab el Mandeb Strait are limited, but a segment of data collected immediately at the approach of the strait (Fig. 1) shown in Fig. 9 reveals a change in stratigraphic character at ~100 ms below the seabed. The flatter stratigraphy (arrowed) and more
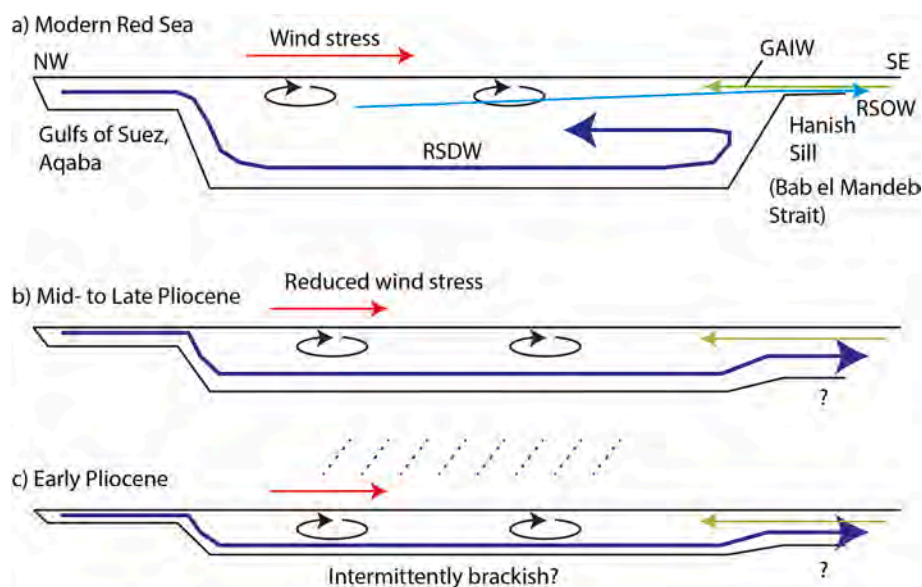
Fig. 8. Schematic illustration of the circulation in (a) the modern Red Sea, (b) proposed for the Mid- to Late Pliocene and (c) early Pliocene. Panel (a) is based on Sofianos and Johns (2015). GAIW: Gulf of Aden Inflow Water, RSDW: Red Sea Deep Water, RSOW: Red Sea Outflow Water. (For interpretation of the references to colour in this figure legend, the reader is referred to the web version of this article.)
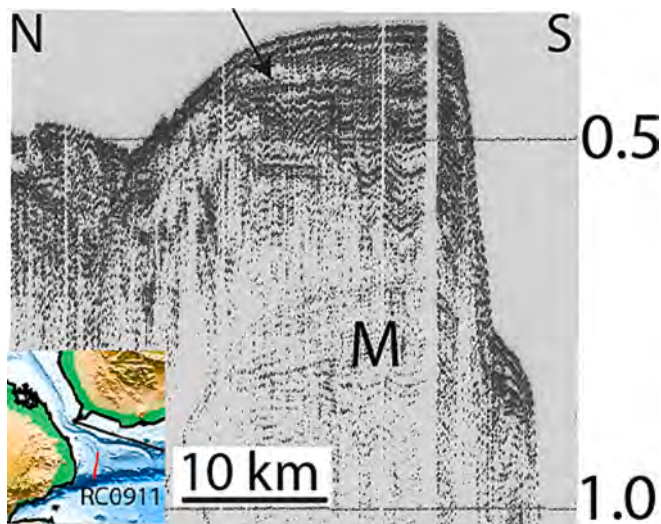
Fig. 9. Seismic reflection image collected on cruise RC0911 at the entrance of Bab el Mandeb Strait. Values to right are seismic two-way times in seconds. Arrow highlights a flat reflection and irregular reflections below it that contrast with the rounded, smooth morphology of the seabed reflection. M: water-column multiple. (A colour version of this figure can be found on the online version of this article.)

irregular reflections immediately below it may indicate different hydraulic conditions. We cannot know its origins exactly, though more rapid RSOW may be one explanation. There appears to have been a change towards more quiescent conditions at the modern seabed, which is smoother. This is consistent with more limited RSOW, which presently passes along the narrow channel immediately north of this line (Fig. 1; Bower et al., 2005).

6.2. Local wind-driven circulations

Could more localised wind-driven surface eddies have affected the seabed and hence played a role in the development of these mounded sedimentary bodies? Recall that many seismic datasets do not reveal mounds, suggesting that they are not widespread. With more exchange of water with the global oceans in the mid-PP, the sea was less density stratified. Wind-driven circulations would have likely penetrated more deeply and may have been able to turn over the whole water column, rather than merely the 200-m surface layer, as eddies are presently constrained by the stratification (Bower and Farrar, 2015). The seabed was also much shallower in the earlier PP (Mitchell et al., 2021), increasing the possibility of the wind-driven circulation reaching the seabed or near to it. Notably, the sediment mounds in profiles D to I are located near to the centres of persistent eddy occurrences in the modern Red Sea and A-B lie under an area of more irregular eddy occurrences (Campbell, 2020).

Wind gaps in the topography surrounding the Red Sea hills control the wind stress on the sea surface (Jiang et al., 2009). As the 5.3 m.y. of the PP is only 1/4 of the time since the main Red Sea rifting stage (Bosworth, 2015), geomorphological changes since the start of the Pliocene are likely to have been modest. We might expect entrenchment along fluvial channels to have been overall less than the uplift of western Arabia due to changing dynamic topography, which has been ~100 m over the Plio-Pleistocene (Wilson et al., 2014; Mitchell et al., 2021). That is small compared with the relief of land, which exceeds 2000 m in parts of Arabia (Fig. 1). The major gap crossing the mountains of west Arabia appears linked to the Qazaz or Najd shear zone (Fig. 1), which is an old shield structure (Stern and Johnson, 2010) and hence a persistent feature. The Tokar is the most important gap on the west side and also overlies an old lithospheric boundary (Stern and Johnson, 2010).

Thermal chronological studies reveal no major change in exhumation over the past 5 m.y. along most of the Red Sea margins (Boone et al., 2021). If wind gaps had similar sizes in the Pliocene as today, it seems possible, to the extent that eddies are controlled by winds (Bower and Farrar, 2015), that they formed at similar locations to today (Fig. 1) and potentially influenced the seabed.

The southward surface current in the buoyancy-driven model of Sofianos and Johns (2003) (Fig. 1) coincides with a strong southward wind jet in summer (Jiang et al., 2009). Those southward winds arise from the Gulf of Suez effectively forming a wind gap between the Red Sea Hills to the west and the high topography of Sinai. As the models of Sofianos and Johns (2003) included a more uniform wind field in the north, incorporating the Gulf of Suez wind jet would likely have enhanced the southward current predicted by their model on the westerly Red Sea coast. The Gulf of Suez has been a persistent geomorphic feature through the Pliocene, evolving only slowly (Steckler and Omar, 1994; Bosworth et al., 2005; Bosworth, 2015). We can expect a southward current to have occurred off the Nubian coast during the Pliocene due to this wind and from the densification of waters around the northern Red Sea discussed earlier, explaining the origins of mound M1.

6.3. Our preferred view for the Plio-Pleistocene Red Sea

The proximity of the mounds in profiles D–I to eddies in the modern Red Sea surface (Fig. 1) suggests an origin from surface eddies. We favour this also because the mounds are not widespread. The gradual changes in the geometries of reflections within them towards the present seabed then reflect the gradual subsidence of the main trough of the Red Sea, removing the seabed from surface influences. It also reflects a gradual increase in stratification of Red Sea waters as the sea became more isolated and as the regional climate became dryer. However, M1 and M2 are not so obviously associated with eddy clusters. Both wind-driven and thermohaline transport may have operated there to form these elongate deposits. In the early Pliocene (Fig. 8c), rainfall and the small sea volume may have led to generally brackish conditions, leading to low carbonate MARs at Site 225 (Fig. 5b). After the climate became generally dryer at ~4.3 Ma (Liddy et al., 2016), the deepening sea became more normal marine in salinity and δ^{18}O, allowing pelagic foraminifera to become established (Fig. 4), with eddies affecting the seabed less strongly (Fig. 8b). The surface eddies then decoupled from the seabed as at the present day (Fig. 8a), leading to mostly pelagic-type deposition. This point may have differed in time around the basin as, for example, it appears higher in the stratigraphy for M1 (Fig. 6b). Sampling the stratigraphy by drilling would allow this important change to be dated. Sampling and dating at sites in the Gulf of Aden immediately southeast of the Bab el Mandeb Strait could potentially date changes in the Red Sea Outflow Waters, as has been successfully done for the Mediterranean outflow (Hernández-Molina et al., 2014).

7. Conclusions

Mounded deposits of sediments in the lower Plio-Pleistocene (PP) in seismic reflection data are interpreted as formed by stronger deep currents than occur today. The dips of the reflections within those bodies grade upwards towards typically flatter reflections around the seabed, suggesting a gradual change in the water circulation that created these bodies. Other evidence suggests that salinities in the middle-late Pliocene Red Sea did not reach such extreme values as they did in the late Pleistocene: aragonite cemented "hard layers" were less common in the Pliocene DSDP cores and seismic data tend to be more transparent in deep waters away from terrigenous sources. For the early Pliocene Red Sea, a wetter regional climate and brackish waters have been reported by others from analyses of sediment samples.

Some of these mounds, particularly those in the northern Red Sea, may be explained by a thermohaline circulation initiated by sea evaporation in marginal gulfs and lagoons. The shallower waters of the

earlier PP flanks of the Red Sea and less density stratification may have also allowed surface currents caused by winds to penetrate more deeply and affect the seabed. In our preferred interpretation, these sedimentary mounds originate largely from wind-driven currents, but enhanced by thermohaline circulation in places, such as along the Egyptian margin (mound M1). The influence of surface currents appears to have declined gradually, leading to reflection geometries that change gradually towards the present seabed.

CRediT authorship contribution statement

Neil C. Mitchell: Writing – review & editing, Writing – original draft, Visualization, Software, Project administration, Methodology, Funding acquisition, Formal analysis, Conceptualization. **Marco Ligi:** Writing – review & editing, Formal analysis. **Jonas Preine:** Writing – review & editing, Formal analysis. **Diederik Liebrand:** Writing – review & editing. **Moamen Ali:** Writing – review & editing, Formal analysis. **Alessandro Decarlis:** Writing – review & editing.

Declaration of competing interest

The authors declare that they have no known competing financial interests or personal relationships that could have appeared to influence the work reported in this paper.

Data availability

The data shown in Fig. 6 are confidential. Copies of the seismic images in Figs. 7 and 9 are provided without annotation in Supplementary Data, along with profile end coordinates. Grids of the top of the S-reflection and thickness of the Plio-Pleistocene sediments can be obtained from https://dx.doi.org/10.26022/IEDA/331395. High-resolution bathymetry grids of the multibeam sonar data shown in Fig. S3a are available from https://doi.pangaea.de/10.1594/PAN-GAEA.860374 and https://doi.pangaea.de/10.1594/PANGAEA.912178.

Acknowledgments

Appendix A. Supplementary data

Supplementary data to this article can be found online at https://doi.org/10.1016/j.gloplacha.2024.104527.

References

Abell, J.T., Winckler, G., Anderson, R.F., Herbert, T.D., 2021. Poleward and weakened westerlies during Pliocene warmth. Nature 589 (7840), 70–75.

Akers, W.H., 1974. Foraminiferal range charts for Arabian Sea and Red Sea sites, Leg 23. In: Davies, T.A., Luyendyk, B.P., et al. (Eds.), Initial Reports of the Deep Sea Drilling Project U.S. Government Printing Office, 26, pp. 1013–1050.

Ali, M., Ligi, M., Ceriani, A., Bouchaala, F., Bosworth, W., Decarlis, A., 2022. Geophysical evidence for magmatism southwest of the Brothers Islands, Northern Red Sea (offshore Quseir, Egypt). Tectonics 41 art. e2022TC007228.

Ali, M., Decarlis, A., Ligi, M., Ball, P., Bosworth, W., Ceriani, A., 2023. Red Sea rifting in Central Egypt: constraints from the offshore Quseir province. J. Geol. Soc. Lond. 180 art. jgs2022-2105.

Almogi-Labin, A., Hemleben, C., Meischner, D., Erlenkeuser, H., 1996. Response of Red Sea deep-water agglutinated foraminifera to water-mass changes during the late Quaternary. Mar. Micropaleontol. 28, 283–297.

Almogi-Labin, A., Hemleben, C., Meischner, D., 1998. Carbonate preservation and climate changes in the Central Red Sea during the last 380 kyr as recorded by pteropods. Mar. Micropaleontol. 33, 87–107.

Álvarez, W., 2023. An enormous Pliocene or Quaternary Megalake Sudd on the River Nile in the Sudan Basin? A review of the dilemma, and a possible solution. J. Afr. Earth Sci. 208 art. 105016.

Angeletti, L., Rasul, N.M.A., Taviani, M., 2019. Mollusc fauna associated with late Pleistocene coral reef systems of the Saudi Arabian side of the Gulf of Aqaba. In: Rasul, N.M.A., Stewart, I.C.F. (Eds.), Geological Setting, Palaeoenvironment and Archaeology of the Red Sea. Springer Earth System Science Series. Springer Nature, Cham, Switzerland, pp. 367–388.

Augustin, N., Devey, C.W., van der Zwan, F.M., Feldens, P., Tominaga, M., Bantan, R., Kwasnitschka, T., 2014. The transition from rifting to spreading in the Red Sea. Earth Planet. Sci. Lett. 395, 217–230.

Augustin, N., van der Zwan, F.M., Devey, C.W., Ligi, M., Kwasnitschka, T., Feldens, P., Bantan, R., Basaham, A.S., 2016. Geomorphology of the Central Red Sea Rift: determining spreading processes. Geomorph 274, 162–179.

Augustin, N., Mitchell, N.C., van der Zwan, F.M., shipboard_scientific_party, 2019. RV Pelagia Fahrtbericht / Cruise Report 64PE-445: SALTAX: Geomorphology and Geophysics of Submarine Salt Flows in the Red Sea Rift, Limassol (Cyprus) – Safaga (Egypt), 27.08. – 21.09.2018. GEOMAR Helmholtz-Zentrum für Ozeanforschung, Kiel, Germany, p. 46.

Bar-Matthews, M., Ayalon, A., Gilmour, M., Matthews, A., Hawkesworth, C.J., 2003. Sea–land oxygen isotopic relationships from planktonic foraminifera and speleothems in the Eastern Mediterranean region and their implication for paleorainfall during interglacial intervals. Geochim. Cosmochim. Acta 67, 3181–3199.

Bar-Yosef, O., Belfer-Cohen, A., 2001. From Africa to Eurasia - early dispersals. Quat. Int. 75, 19–28.

Beal, L.M., Ffield, A., Gordon, A.L., 2000. Spreading of Red Sea overflow waters in the Indian Ocean. J. Geophys. Res. 105, 8549–8564.

Becker, J.J., Sandwell, D.T., Smith, W.H.F., Braud, J., Binder, B., Depner, J., Fabre, D., Factor, J., Ingalls, S., Kim, S.-H., Ladner, R., Marks, K., Nelson, S., Pharaoh, A., Trimmer, R., Von Rosenberg, J., Wallace, G., Weatherall, P., 2009. Global Bathymetry and Elevation Data at 30 Arc seconds Resolution: SRTM30_PLUS. Mar. Geod. 32, 355–371.

Biton, E., Hildor, H., Peltier, W.R., 2008. Red Sea during the last Glacial Maximum: implications for sea level reconstruction. Paleocean 23 art. PA1214. doi:1210.1029/2007PA001431.

Bode, G.W., 1974a. Appendix I. Grain-size analyses, Leg 23. In: Whitmarsh, R.B., Weser, O.E., Ross, D.A., et al. (Eds.), Initial Reports of the Deep Sea Drilling Project U.S. Government Printing Office, 23, pp. 1127–1130.

Bode, G.W., 1974b. Appendix II. Carbon and carbonate analyses, Leg 23. In: Whitmarsh, R.B., Weser, O.E., Ross, D.A., et al. (Eds.), Initial Reports of the Deep Sea Drilling Project U.S. Government Printing Office, 23, pp. 1131–1135.

Bonatti, E., Colantoni, P., Della Vedova, B., Gelmini, G., Marinelli, G., Pospischl, D., Rossi, S., Taviani, M., 1981. Geology of the Red Sea between 23° and 25° N` preliminary results. Oceanol. Acta 47, 607–613.

Bonatti, E., Colantoni, P., Della Vedova, B., Taviani, M., 1984. Geology of the Red Sea transitional zone (22°N-25°N). Oceanol. Acta 7, 385–398.

Boone, S.C., Balestieri, M.L., Kohn, B., 2021. Tectono-thermal evolution of the Red Sea Rift. Front. Earth Sci. 9 art. 713448.

Bosworth, W., 2015. Geological evolution of the Red Sea: Historical background, review and synthesis. In: Rasul, N.M.A., Stewart, I.C.F. (Eds.), The Red Sea: The Formation, Morphology, Oceanography and Environment of a Young Ocean Basin. Springer Earth System Sciences, Berlin Heidelberg.

Bosworth, W., Huchon, P., McClay, K., 2005. The Red Sea and Gulf of Aden basins. J. Afr. Earth Sci. 43, 334–378.

Bouilloux, A., Valet, J.-P., Bassinot, F., Joron, J.-L., Dewilde, F., Blanc-Valleron, M.-M., Moreno, E., 2013. Influence of seawater exchanges across the Bab-el-Mandeb Strait on sedimentation in the Southern Red Sea during the last 60 ka. Paleocean 28, 675–687 doi:610.1002/2013PA002544.

Bower, A.S., Farrar, J.T., 2015. Air-sea interaction and horizontal circulation in the Red Sea. In: Rasul, N.M.A., Stewart, I.C.F. (Eds.), The Red Sea: The Formation, Morphology, Oceanography and Environment of a Young Ocean Basin. Springer Earth System Sciences, Berlin, Heidelberg, pp. 329–342.

Bower, A.S., Johns, W.E., Fratantoni, D.M., Peters, H., 2005. Equilibration and circulation of Red Sea Outflow Water in the Western Gulf of Aden. J. Phys. Oceanogr. 35, 1963–1985.

Brierley, C.M., Fedorov, A.V., Liu, Z., Herbert, T.D., Lawrence, K.T., LaRiviere, J.P., 2009. Greatly expanded tropical warm pool and weakened Hadley circulation in the early Pliocene. Science 323, 1714–1718.

Briggs, L.I., 1958. Evaporite facies. J. Sediment. Petrol. 28, 46–56.

Campbell, M.F., 2020. Mesoscale Eddy Dynamics and Scale in the Red Sea. King Abdullah University of Science and Technology, Thuwal, Saudi Arabia, p. 150. PhD thesis.

Caruso, A., Cita, M.B., Marino, M., Maiorano, P., Scopelliti, G., Blanc-Valleron, M.-M., 2013. Paleoceanographic and paleoenvironmental changes in the Red Sea during the Messinian/Zanclean: New data from Site 225 (abstract). In: Cagatay, N., Zabci, C. (Eds.), Regional Committee on Mediterranean Neogene Stratigraphy 14th Congress: Neogene to Quaternary Geological Evolution of Mediterranean, Paratethys and Black Sea. Istanbul Technical University, Istanbul, p. 57.

Cember, R.P., 1988. On the sources, formation, and circulation of Red Sea deep water. J. Geophys. Res. 93, 8175–8191.

Chacko, T., Deines, P., 2008. Theoretical calculation of oxygen isotope fractionation factors in carbonate systems. Geochim. Cosmochim. Acta 72, 3642–3660.

Chen, C., Li, R., Pratt, L., Limeburner, R., Beardsley, R.C., Bower, A., Jiang, H., Abualnaja, Y., Xu, Q., Lin, H., Liu, X., Lan, J., Kim, T., 2014. Process modeling studies of physical mechanisms of the formation of an anticyclonic eddy in the Central Red Sea. J. Geophys. Res. 119, 1445–1464 doi:1410.1002/2013JC009351.

Chu, D., Gordon, R.G., 1998. Current plate motions across the Red Sea. Geophys. J. Int. 135, 313–328.

Clifford, M., Horton, C., Schmitz, J., Kantha, L.H., 1997. An oceanographic nowcast/ forecast system for the Red Sea. J. Geophys. Res. 102, 25101–25122.

Cochran, J., Gaulier, J.-M., LePichon, X., 1991. Crustal structure and the mechanism of extension in the Northern Red Sea: constraints from gravity anomalies. Tectonics 10, 1018–1037.

Cochran, J.R., 2005. Northern Red Sea: Nucleation of an oceanic spreading center within a continental rift. Geochem. Geophys. Geosyst. 6 art. Q03006, doi:03010.01029/ 02004GC000826.

Coleman, R.G., 1974. Geologic background of the Red Sea. In: Whitmarsh, R.B., Weser, O.E., Ross, D.A., et. al. (Eds.), Initial Reports of the Deep Sea Drilling Project, vol. 23. U.S. Govt. Printing Office, Washington, D.C., pp. 813–819

Colombo, D., McNeice, G., Raterman, N., Zinger, M., Rovetta, D., Sandoval Curiel, E., 2014. Exploration beyond seismic: the role of electromagnetics and gravity gradiometry in deep water subsalt plays of the Red Sea. Interpretation 2. SH33-SH53.

Coplen, T.B., Kendall, C., Hopple, J., 1983. Comparison of stable isotope reference samples. Nature 302, 236–238.

Dambricourt Malassé, A., 2016. The first Indo-French Prehistorical Mission in Siwaliks and the discovery of anthropic activities at 2.6 million years. Compte. Rendus Palevol. 15, 281–294.

Davison, I., Al-Kadashi, M., Al-Khirbash, S., Al-Subbary, A.K., Baker, J., Blakey, S., Bosence, D., Dart, C., Heaton, R., McClay, K., Menzies, M., Nichols, G., Owen, L., Yellend, J., 1994. Geological evolution of the southeastern Red Sea Rift margin, Republic of Yemen. Geol. Soc. Am. Bull. 106, 1474–1493.

Delaunay, A., Baby, G., Fedorik, J., Afifi, A.M., Tapponnier, P., Dyment, J., 2023. Structure and morphology of the Red Sea, from the mid-ocean ridge to the ocean-continent boundary. Tectonophys 849 art. 229728.

Dowsett, H., Thompson, R., Barron, J., Cronin, T., Fleming, F., Ishman, S., Poore, R., Willard, D., Holtz, T., 1994. Joint investigations of the Middle Pliocene climate I: PRISM paleoenvironmental reconstructions. Glob. Planet. Chang. 9 (− 3), 169–195.

Dowsett, H.J., Foley, K.M., Stoll, D.K., Chandler, M.A., Sohl, L.E., Bentsen, M., Otto-Bliesner, B.L., Bragg, F.J., Chan, W.-L., Contoux, C., Dolan, A.M., Haywood, A.M., Jonas, J.A., Jost, A., Kamae, Y., Lohmann, G., Lunt, D.J., Nisancioglu, K.H., Abe-Ouchi, A., Ramstein, G., Riesselman, C.R., Robinson, M.M., Rosenbloom, N.A., Salzmann, U., Stepanek, C., Strother, S.L., Ueda, H., Yan, Q., Zhang, Z., 2013. Sea surface temperature of the mid-Piacenzian Ocean: a data-model comparison. Sci. Report. 3 art. srep02013.

Ehrhardt, A., Hübscher, C., 2015. The northern Red Sea in transition from rifting to drifting - lessons learned from ocean deeps. In: Rasul, N.M.A., Stewart, I.C.F. (Eds.), The Red Sea: The Formation, Morphology, Oceanography and Environment of a Young Ocean Basin. Springer Earth System Sciences, Berlin Heidelberg, pp. 99–121.

Ehrhardt, A., Hübscher, C., Gajewski, D., 2005. Conrad deep, Northern Red Sea: Development of an early stage ocean deep within the axial depression. Tectonophys 411, 19–40.

Einsele, G., Werner, F., 1972. Sedimentary processes at the entrance Gulf of Aden / Red Sea. In: Seibold, E., Closs, H. (Eds.), "Meteor" Forschungsergebnisse. Reihe C. Bornträger, Berlin, pp. 39–62.

Eppelbaum, L.V., Katz, Y.I., 2022. Combined zonation of the African-Levantine-Caucasian areal of ancient hominin: Review and integrated analysis of paleogeographical, stratigraphic and geophysical-geodynamical data. Geosciences 12 art. 21.

Faris, M., Farouk, S., Jain, S., Shabaan, M., 2023. Miocene–Pliocene calcareous nannofossil biostratigraphy and bioevents in Egypt. J. Afr. Earth Sci. 202, 104862.

Faugères, J.-C., Stow, D.A.V., Imbert, P., Viana, A., 1999. Seismic features diagnostic of contourite drifts. Mar. Geol. 162, 1–38.

Feldens, P., Mitchell, N.C., 2015. Salt flows in the Central Red Sea. In: Rasul, N.M.A., Stewart, I.C.F. (Eds.), The Red Sea: The Formation, Morphology, Oceanography and Environment of a Young Ocean Basin. Springer Earth System Sciences, Berlin Heidelberg, pp. 205–218.

Feldens, P., Schmidt, M., Mücke, I., Augustin, N., Al-Farawati, R., Orif, M., Faber, E., 2016. Expelled subsalt fluids form a pockmark field in the eastern Red Sea. Geo-Mar. Lett. 36, 339–352.

Fenton, M., Geiselhart, S., Rohling, E.J., Hemleben, C., 2000. Aplanktonic zones in the Red Sea. Mar. Micropaleontol. 40, 277–294.

Fleisher, R.L., 1974. Preliminary report on late Neogene Red Sea foraminifera, Deep Sea Drilling Project, Leg 23B. In: Davies, T.A., Luyendyk, B.P., et al. (Eds.), Initial reports of the Deep Sea Drilling Project U.S. Government Printing Office, 26, pp. 985–1011.

Fleitmann, D., Burns, S.J., Pekala, M., Mangini, A., Al-Subbary, A., Al-Aowah, M., Kramers, J., Matter, A., 2011. Holocene and Pleistocene pluvial periods in Yemen, southern Arabia. Quat. Sci. Rev. 30, 783–787.

Flood, R.D., 1988. A lee wave model for deep-sea mudwave activity. Deep-Sea Res. 35, 973–983.

Garcia, T., Féraud, G., Falguède Lumley, C., Perrenoud, C., Lordkipanidze, D., 2010. Earliest human remains in Eurasia: new $^{40}Ar/^{39}Ar$ dating of the Dmanisi hominid-bearing levels, Georgia. Quat. Geochronol. 5, 443–451.

Gass, I.G., Mallick, D.I.J., Cox, K.G., 1973. Volcanic islands of the Red Sea. J. Geol. Soc. 129, 275–310.

Gemmer, L., Ings, S.J., Medvedev, S., Beaumont, C., 2004. Salt tectinics driven by differential sediment loading: stability analysis and finite element experiments. Basin Res. 16, 199–218.

Gordon, G., Hansen, B., Scott, J., Hirst, C., Graham, R., Grow, T., Spedding, A., Fairhead, S., Fullarton, L., Griffin, O., 2010. The hydrocarbon prospectivity of the Egyptian North Red Sea basin. In: Vining, B.A., Pickering, S.C. (Eds.), Petroleum Geology: From Mature Basins to New Frontiers - Proceedings of the 7th Petroleum Geology Conference. Geol. Soc. Lond., London, pp. 783–789. https://doi.org/ 10.1144/0070783.

Grant, K.M., Rohling, E.J., Bronk Ramsey, C., Cheng, H., Edwards, R.L., Florindo, F., Heslop, D., Marra, F., Roberts, A.P., Tamisiea, M.E., Williams, F., 2014. Sea-level variability over five glacial cycles. Nat. Commun., 5076 https://doi.org/10.1038/ ncomms6076.

Grant, K.M., Amarathunga, U., Amies, J.D., Hu, P., Qian, Y., Penny, T., Laura Rodriguez-Sanz, L., Zhao, X., Heslop, D., Liebrand, D., Hennekam, R., Westerhold, T., Gilmore, S., Lourens, L.J., Roberts, A.P., Rohling, E.J., 2022. Organic carbon burial in Mediterranean sapropels intensified during Green Sahara periods since 3.2 Myr ago. Commun. Earth & Env. 3 art. s43247-43021-00339-43249.

Guennoc, P., Pautot, G., Coutelle, A., 1988. Surficial structures of the northern Red Sea axial valley from 23°N to 28°N: time and space evolution of neo-oceanic structures. Tectonophys 153, 1–23.

Hemleben, C., Meischner, D., Zahn, R., Almogi-Labin, A., Erlenkeuser, H., Hiller, B., 1996. Three hundred eighty thousand year long stable isotope and faunal records from the Red Sea: influence of global sea level change on hydrography. Paleoceanography 11, 147–156.

Hernández-Molina, F.J., Stow, D.A.V., Alvarez-Zarikian, C.A., Acton, G., Bahr, A., Balestra, B., Ducassou, E., Flood, R., Flores, J.-A., Furota, S., Grunert, P., Hodell, D., Jimenez-Espejo, F., Kim, J.K., Krissek, L., Kuroda, J., Li, B., Llave, E., Lofi, J., Lourens, L., Miller, M., Nanayama, F., Nishida, N., Richter, C., Roque, C., Pereira, H., Sanchez Goñi, M.F., Sierro, F.J., Singh, A.D., Sloss, C., Takashimizu, Y., Tzanova, A., Voelker, A., Williams, T., Xuan, C., 2014. Onset of Mediterranean outflow into the North Atlantic. Science 344, 1244–1250.

Hernández-Molina, F.J., Wåhlin, A., Bruno, M., Ercilla, G., Llave, E., Serra, N., Rosón, G., Puig, P., Rebesco, M., Van Rooij, D., Roque, D., González-Pola, C., Sánchez, F., Gómez, M., Preu, B., Schwenk, T., Hanebuth, T.J.J., Sánchez Leal, R.F., García-Lafuente, J., Brackenridge, R.E., Juan, C., Stow, D.A.V., Sánchez-González, J.M., 2016. Oceanographic processes and morphosedimentary products along the Iberian margins: a new multidisciplinary approach. Mar. Geol. 378, 127–156.

Horowitz, A., 1989. Continuous pollen diagrams for the last 3.5 M.Y. From Israel: vegetation, climate and correlation with the oxygen isotope record. Palaeogeogr. Palaeoclimatol. Palaeoecol. 72, 63–78.

Hughes, G.W., Johnson, R.S., 2005. Lithostratigraphy of the Red Sea Region. GeoArabia 10, 49–126.

Hughes, G.W., Varol, O., 2024. Biostratigraphically constrained Neogene palaeoenvironments of the Red Sea rift complex. In: Rasul, N.M.A., Stewart, I.C.F. (Eds.), Rifting and Sediments in the Red Sea and Arabian Gulf Regions. Taylor & Francis, pp. 324–341.

Hughes, G.W., Abdine, S., Girgis, M.H., 1992. Miocene biofacies development and geological history of the Gulf of Suez, Egypt. Mar. Pet. Geol. 9, 2–28.

Izzeldin, A.Y., 1987. Seismic, gravity and magnetic surveys in the central part of the Red Sea: their interpretation and implications for the structure and evolution of the Red Sea. Tectonophysics 143, 269–306.

Jarosz, E., Murray, S.P., Inoue, M., 2005. Observations on the characteristics of tides in the Bab el Mandab Strait. J. Geophys. Res. 110 art. C03015, doi:03010.01029/ 02004JC002299.

Jiang, H., Farrar, J.T., Beardsley, R.C., Chen, R., Chen, C., 2009. Zonal surface wind jets across the Red Sea due to mountain gap forcing along both sides of the Red Sea. Geophys. Res. Lett. 36 art. L19605, doi:19610.11029/12009GL040008.

Jung, S.J.A., Ganssen, G.M., Davies, G.R., 2001. Multidecadal variations in the early Holocene outflow of Red Sea Water into the Arabian Sea. Paleocean 16 art. 6570668.

Kawagata, S., Hayward, B.W., Gupta, A.K., 2006. Benthic foraminiferal extinctions linked to late Pliocene–Pleistocene deep-sea circulation changes in the northern Indian Ocean (ODP Sites 722 and 758). Mar. Micropaleontol. 58, 219–242.

Kim, J., Kimura, Y., Puchala, B., Yamazaki, T., Becker, U., Sun, W., 2023. Dissolution enables dolomite crystal growth near ambient conditions. Science 382, 915–920.

Klein, E.M., Langmuir, C.H., 1987. Global correlations of ocean ridge basalt chemistry with axial depth and crustal thickness. J. Geophys. Res. 92, 8089–8115.

Kopp, G.H., Roos, C., Butynski, T.M., Wildman, D.E., Alagaili, A.N., Groeneveld, L.F., Zinner, D., 2014. Out of Africa, but how and when? The case of hamadryas baboons (*Papio hamadryas*). J. Hum. Evol. 76, 154–164.

Lambeck, K., Purcell, A., Flemming, N.C., Vita-Finzi, C., Alsharekh, A.M., Bailey, G.N., 2011. Sea level and shoreline reconstructions for the Red Sea: isostatic and tectonic considerations and implications for hominin migration out of Africa. Quat. Sci. Rev. 30, 3542–3574.

Lane-Serff, G.F., Smeed, D.A., Postlethwaite, C.R., 2000. Multi-layer hydraulic exchange flows. J. Fluid Mech. 416, 269–296.

Larrasoaña, J.C., Roberts, A.P., Rohling, E.J., 2013. Dynamics of Green Sahara periods and their role in hominin evolution. PLoS One 8 art. e76514.

Lawrence, J.R., 1974. Stable oxygen and carbon isotope variations in the pore waters, carbonates and silicates, Sites 225 and 228, Red Sea. In: Whitmarsh, R.B., Weser, O. E., Ross, D.A., et al. (Eds.), Initial Reports of the Deep Sea Drilling Project, 23. U.S. Govt. Printing Office, Washington, D.C., pp. 939–942

Lehner, B., Grill, G., 2013. Global river hydrography and network routing: baseline data and new approaches to study the world's large river systems. Hydrol. Process. 27, 2171–2186.

Li, X., Jiang, D., Zhang, Z., Zhang, R., Tian, Z., Yan, Q., 2015. Mid-Pliocene westerlies from PlioMIP simulations. Adv. Atmos. Sci. 32 (7), 909–923.

Li, X., Jiang, D., Tian, Z., Yang, Y., 2018. Mid-Pliocene global land monsoon from PlioMIP1 simulations. Palaeogeogr. Palaeoclimatol. Palaeoecol. 512, 56–70.

Liddy, H.M., Feakins, S.J., Tierney, J.E., 2016. Cooling and drying in Northeast Africa across the Pliocene. Earth Planet. Sci. Lett. 449, 430–438.

Ligi, M., Bonatti, E., Tontini, F.C., Cipriani, A., Cocchi, L., Schettino, A., Bortoluzzi, G., Ferrante, V., Khalil, S., Mitchell, N.C., Rasul, N., 2011. Initial burst of oceanic crust accretion in the Red Sea due to edge-driven mantle convection. Geology 39, 1019–1022.

Ligi, M., Bonatti, E., Bortoluzzi, G., Cipriani, A., Cocchi, L., Caratori Tontini, F., Carminati, E., Ottolini, L., Schettino, A., 2012. Birth of an ocean in the Red Sea: initial pangs. Geochem. Geophys. Geosyst. 13 art. Q08009, doi:08010.01029/ 02012GC004155.

Ligi, M., Bonatti, E., Bosworth, W., Cai, Y., Cipriani, A., Palmiotto, C., Ronca, S., Seyler, M., 2018. Birth of an ocean in the Red Sea: Oceanic-type basaltic melt intrusions precede continental rupture. Gondwana Res. 54, 150–160.

Ligi, M., Bosworth, W., Ronca, S., 2019. Oceanization starts at depth during continental rupturing in the Northern Red Sea. In: Rasul, N.M.A., Stewart, I.C.F. (Eds.), Geological Setting, Palaeoenvironment and Archaeology of the Red Sea. Springer Nature Switzerland, Cham, Switzerland, pp. 131–157.

Maillard, C., Soliman, G., 1986. Hydrography of the Red Sea and exchanges with the Indian Ocean in summer. Oceanol. Acta 9, 249–269.

Mallick, D.I.J., Gass, I.G., Cox, K.G., de Vries, B.V.W., Tindle, A.G., 1990. Perim Island, a volcanic remnant in the southern entrance to the Red Sea. Geol. Mag. 127, 309–318.

Manheim, F.T., 1974. Red Sea geochemistry. In: Whitmarsh, R.B., Weser, O.E., Ross, D. A., et al. (Eds.), Initial Reports of the Deep Sea Drilling Project, 23. U.S. Govt. Printing Office, Washington, D.C., pp. 975–998

Manheim, F.T., Dwight, L., Belastock, R.A., 1974. Porosity, density, grain density, and related physical properties of sediments from the Red Sea drill cores. In: Whitmarsh, R.B., Weser, O.E., Ross, D.A., et al. (Eds.), Initial Reports of the Deep Sea Drilling Project, 23. U.S. Govt. Printing Office, Washington, D.C., pp. 887–907

Martinez, F., Cochran, J.R., 1988. Structure and tectonics in the northern Red Sea: catching a continental margin between rifting and drifting. Tectonophys 150, 1–32.

Matter, A., Neubert, E., Preusser, F., Rosenberg, T., Al-Wagdani, A., 2015. Palaeo-environmental implications derived from lake and sabkha deposits of the southern Rub' al-Khali, Saudi Arabia and Oman. Quat. Int. 382, 120–131.

McClusky, S., Reilinger, R., Mahmoud, S., Ben Sari, D., Tealeb, A., 2003. GPS constraints on Africa (Nubia) and Arabia plate motions. Geophys. J. Int. 155, 126–138.

Messager, E., Nomade, S., Voinchet, P., Ferring, R., Mgeladze, A., Guillou, H., Lordkipanidze, D., 2011. ^{40}Ar/^{39}Ar dating and phytolith analysis of the early Pleistocene sequence of Kvemo-Orozmani (Republic of Georgia): chronological and palaeoecological implications for the hominin site of Dmanisi. Quat. Sci. Rev. 30, 3099–3108.

Milliman, J.D., Ross, D.A., Ku, T.-L., 1969. Precipitation and lithification of deep-sea carbonates in the Red Sea. J. Sediment. Petrol. 39, 724–736.

Mitchell, N.C., Augustin, N., 2017. Halokinetics and other features of GLORIA long-range sidescan sonar data from the Red Sea. Mar. Pet. Geol. 88, 724–738.

Mitchell, N.C., Bosworth, W., 2024. The tectonic stability of Arabia. In: Rasul, N.M.A., Stewart, I.C.F. (Eds.), Rifting and Sediments in the Red Sea and Arabian Gulf Regions. Taylor & Francis, pp. 57–94.

Mitchell, N.C., Huthnance, J.M., 2013. Geomorphological and geochemical evidence (^{230}Th anomalies) for cross-equatorial currents in the Central Pacific. Deep-Sea Res. I 78, 24–41.

Mitchell, N.C., Sofianos, S.S., 2019. Origin of submarine channel north of Hanish Sill, Red Sea. In: Rasul, N.M.A., Stewart, I.C.F. (Eds.), Geological Setting, Palaeoenvironment and Archaeology of the Red Sea. Springer Earth System Science Series. Springer Nature, Cham, Switzerland, pp. 259–274.

Mitchell, N.C., Ligi, M., Farrante, V., Bonatti, E., Rutter, E., 2010. Submarine salt flows in the Central Red Sea. Geol. Soc. Am. Bull. 122, 701–713.

Mitchell, N.C., Ligi, M., Rohling, E.J., 2015. Red Sea isolation history suggested by Plio-Pleistocene seismic reflection sequences. Earth Planet. Sci. Lett. 430, 387–397.

Mitchell, N.C., Ligi, M., Feldens, P., Hübscher, C., 2017. Deformation of a young salt giant: regional topography of the Red Sea Miocene evaporites. Basin Res. 29, 352–369.

Mitchell, N.C., Ligi, M., Rasul, N.M.A., 2019. Variations in Plio-Pleistocene deposition in the Red Sea. In: Rasul, N.M.A., Stewart, I.C.F. (Eds.), Geological Setting, Palaeoenvironment and Archaeology of the Red Sea. Springer Earth System Science Series. Springer Nature, Cham, Switzerland, pp. 323–340.

Mitchell, N.C., Shi, W., Izzeldin, A.Y., Stewart, I.C.F., 2021. Reconstructing the level of the Central Red Sea evaporites at the end of the Miocene. Basin Res. 33, 1266–1292 doi:1210.1111/bre.12513.

Mitchell, N.C., Hernandez, K., Preine, J., Ligi, M., Augustin, N., Izzeldin, A., Hübscher, C., 2022. Early stage diapirism in the Red Sea deep-water evaporites: origins and length-scales. Tectonophys 831 art. 229331.

Neumann, A.C., McGill, D.A., 1962. Circulation of the Red Sea in early summer. Deep-Sea Res. 8, 223–235.

Nicholls, J.F., Toumi, R., Stenchikov, G., 2015. Effects of unsteady mountain-gap winds on eddies in the Red Sea. Atmos. Sci. Lett. 16, 279–284.

Nicholson, S.L., Pike, A.W.G., Hosfield, R., Roberts, N., Sahy, D., Woodhead, J., Cheng, H., Edwards, R.L., Affolter, S., Leuenberger, M., Burns, S.J., Matter, A., Fleitmann, D., 2020. Pluvial periods in Southern Arabia over the last 1.1 million-years. Quat. Sci. Rev. 229 art. 106112.

Okwokwo, O.I., Mitchell, N.C., Shi, W., Stewart, I.C.F., Izzeldin, A.Y., 2022. How have thick evaporites affected early sea-floor spreading magnetic anomalies in the Central Red Sea? Geophys. J. Int. 229, 1550–1566.

Orszag-Sperber, F., Harwood, G., Kendall, A., Purser, B.H., 1998a. Review of the evaporites of the Red Sea-Gulf of Suez rift. In: Purser, B.H., Bosence, D.W.J. (Eds.), Sedimentation and Tectonics of Rift Basins: Red Sea-Gulf of Aden. Chapman & Hall, London, pp. 409–426.

Orszag-Sperber, F., Purser, B.H., Rioual, M., Plaziat, J.-C., 1998b. Post-Miocene sedimentation and rift dynamics in the southern Gulf of Suez and northern Red Sea. In: Purser, B.H., Bosence, D.W.J. (Eds.), Sedimentation and Tectonics of Rift Basins: Red Sea-Gulf of Aden. Chapman & Hall, London, pp. 427–447.

Phillips, J.D., Ross, D.A., 1970. Continuous seismic reflexion profiles in the Red Sea. Philos. Transact. Roy. Soc. 267 (series A), 143–152.

Pierre, C., Caruso, A., Blanc-Valleron, M.-M., Rouchy, J.-M., Orzsag-Sperber, F., 2006. Reconstruction of the paleoenvironmental changes around the Miocene-Pliocene boundary along a West-East transect across the Mediterranean. Sediment. Geol. 188-189, 319–340.

Plaziat, J.-C., Baltzer, F., Choukri, A., Conchon, O., Freytet, P., Orszag-Sperber, F., Raguideau, A., Purser, B.H., 1998. Quaternary marine and continental sedimentation in the northern Red Sea and Gulf of Suez (Egyptian coast): Influences of rift tectonics, climatic changes and sea-level fluctuations. In: Purser, B.H., Bosence, D.W. J. (Eds.), Sedimentation and Tectonics of Rift Basins: Red Sea-Gulf of Aden. Chapman & Hall, London, pp. 537–573.

Pocknall, D.T., Krebs, W.N., Tawfik, E., Ahmed, A.A., 1999. Pliocene climate and depositional environments, Gulf of Suez, Egypt: evidence from palynology and diatoms. In: Wrenn, J.H., Sue, J.-P., Leroy, S.A.G. (Eds.), The Pliocene: Time of Change. American Association of Stratigraphic Palynologists Foundation, pp. 163–171.

Pratt, L.J., Johns, W., Murray, S.P., Katsumata, K., 1999. Hydraulic interpretation of direct velocity measurements in the Bab el Mandab. J. Phys. Oceanogr. 29, 2769–2784.

Purser, B.H., Hötzl, H., 1988. The sedimentary evolution of the Red Sea rift: a comparison of the northwest (Egyptian) and northeast (Saudi Arabian) margins. Tectonophys 153, 193–208.

Quadfasel, D., Baudner, H., 1993. Gyre-scale circulation cells in the Red Sea. Oceanol. Acta 16, 221–229.

Ranganathan, V., 1991. Salt diffusion in interstitial waters and halite removal from sediments: examples from the Red Sea and Illinois basins. Geochim. Cosmochim. Acta 55, 1615–1625.

Rebesco, M., Hernández-Molina, J., Van Rooij, D., Wåhlin, A., 2014. Contourites and associated sediments controlled by deep-water circulation processes: State-of-the-art and future considerations. Mar. Geol. 352, 111–154.

Reilinger, R., McClusky, S., ArRajehi, A., 2015. Geodetic constraints on the geodynamic evolution of the Red Sea. In: Rasul, N.M.A., Stewart, I.C.F. (Eds.), The Red Sea: The Formation, Morphology, Oceanography and Environment of a Young Ocean Basin. Springer Earth System Sciences. Springer Earth System Sciences, Berlin Heidelberg, pp. 135–150.

Richter, H., Makris, J., Rihm, R., 1991. Geophysical observations offshore Saudi Arabia: seismic and magnetic observations. Tectonophys 198, 297–310.

Rifai, R.I., 2007. Reconstruction of the Middle Pleistocene climate of South Mediterranean using the Wadi Sannur speleothem, eastern Desert, Egypt. Carbonates Evaporites 22, 73–85.

Rio, D., Sprovieri, R., Castradori, D., Di Stefano, E., 1998. The Gelasian Stage (Upper Pliocene): a new unit of the global standard chronostratigraphic scale. Episodes 21, 82–87.

Rogers, N.W., 1993. The isotope and trace element geochemistry of basalts from the volcanic islands of the southern Red Sea. In: Prichard, H.M., Alabaster, T., Harris, N. B.W., Neary, C.R. (Eds.), Magmatic Processes and Plate Tectonics, Geol. Soc. Lond. Spec. Publ, vol. 76, pp. 455–467.

Rohling, E.J., Fenton, M., Jorissen, F.J., Bertrand, P., Ganssen, G., Caulet, J.P., 1998. Magnitudes of sea-level lowstands of the past 500,000 years. Nature 394, 162–165.

Rohling, E.J., Grant, K., Bolshaw, M., Roberts, A.P., Siddall, M., Hemleben, C., Kucera, M., 2009. Antarctic temperature and global sea level closely coupled over the past five glacial cycles. Nat. Geosci. 2, 500–504.

Rohling, E.J., Foster, G.L., Grant, K.M., Marino, G., Roberts, A.P., Tamisiea, M.E., Williams, F., 2014. Sea-level and deep-sea-temperature variability over the past 5.3 million years. Nature 508, 477–482.

Ron, H., Levi, S., 2001. When did hominids first leave Africa? New high-resolution magnetostratigraphy from the Erk-el-Ahmar Formation, Israel. Geology 29, 887–890.

Rosenberg, T.M., Preusser, F., Risberg, J., Plikk, A., Kadi, K.A., Matter, A., Fleitmann, D., 2013. Middle and late Pleistocene humid periods recorded in palaeolake deposits of the Nafud desert, Saudi Arabia. Quat. Sci. Rev. 70, 109–123.

Ross, D.A., Schlee, J., 1973. Shallow structure and geologic development of the southern Red Sea. Geol. Soc. Am. Bull. 84, 3827–3848.

Rowan, M.G., 2014. Passive-margin salt basins: hyperextension, evaporite deposition, and salt tectonics. Basin Res. 26, 154–182.

Rowan, M.G., Urai, J.L., Fiduk, J.C., Kukla, P.A., 2019. Deformation of intrasalt competent layers in different modes of salt tectonics. Solid Earth 10, 987–1013.

Schmidt, M., Devey, C., Eisenhauer, A., cruise_participants, 2011. FS Poseidon cruise report P408. Christian-Albrechts University of Kiel, Kiel, Germany.

Schock, S.G., LeBlanc, L.R., Mayer, L.A., 1989. Chirp subbottom profiler for quantitative sediment analysis. Geophysics 54, 445–450.

Searle, R.C., 1980. R.R.S. Discovery Cruise 103, 9–25 July 1979, Geology and Geophysics in the Gulf of Aden and Red Sea, Cruise Report no 88. Institute of Oceanographic Sciences, UK (NERC).

Shanmugam, G., 2017. Contourites: Physical oceanography, process sedimentology, and petroleum geology. Petrol. Expl. Dev. 44, 183–216.

Shi, W., Mitchell, N.C., Kalnins, L., Izzeldin, A.Y., 2018. Oceanic-like axial crustal high in the Central Red Sea. Tectonophys 747-748, 327–342.

Siddall, M., Rohling, E.J., Almogi-Labin, A., Hemleben, C., Meischner, D., Schmeizer, I., Smeed, D.A., 2003. Sea-level fluctuations during the last glacial cycle. Nature 423, 853–858.

Siddall, M., Smeed, D.A., Hemleben, C., Rohling, E.J., Schmeizer, I., Peltier, W.R., 2004. Understanding the Red Sea response to sea level. Earth Panet. Sci. Lett. 225, 421–434.

Smeed, D.A., 2000. Hydraulic control of three-layer exchange flows: application to the Bab al Mandab. J. Phys. Oceanogr. 30, 2574–2588.

Smeed, D.A., 2004. Exchange through the Bab el Mandab. Deep-Sea Res. II 51, 455–474.

Sofianos, S., Johns, W.E., 2015. Water mass formation, overturning circulation, and the exchange of the Red Sea with adjacent basins. In: Rasul, N.M.A., Stewart, I.C.F. (Eds.), The Red Sea: The Formation, Morphology, Oceanography and Environment of a Young Ocean Basin. Springer Earth System Sciences, Berlin Heidelberg, pp. 343–353.

Sofianos, S.S., Johns, E.W., 2003. An Oceanic General Circulation Model (OGCM) investigation of the Red Sea circulation, 2. Three-dimensional circulation in the Red Sea. J. Geophys. Res. 107 art. 3066, doi:3010.1029/2001JC001185.

Sofianos, S.S., Johns, E.W., 2007. Observations of the summer Red Sea circulation. J. Geophys. Res. 112 art. C06025, doi:06010.01029/02006JC003886.

Steckler, M.S., Omar, G.I., 1994. Controls on erosional retreat of the uplifted rift flanks at the Gulf of Suez and northern Red Sea. J. Geophys. Res. 99, 12,159–112,173.

Stern, R.J., Johnson, P., 2010. Continental lithosphere of the Arabian Plate: a geologic, petrologic, and geophysical synthesis. Earth Sci. Rev. 101, 29–67.

Stoffers, P., Ross, D.A., 1974. Sedimentary history of the Red Sea. In: Whitmarsh, R.B., Weser, O.E., Ross, D.A., et al. (Eds.), Initial reports of the Deep Sea Drilling Project U. S. Government Printing Office, 23, pp. 849–865.

Supko, P.R., Stoffers, P., Coplen, T., 1974. Petrography and geochemistry of Red Sea dolomite. In: Whitmarsh, R.B., Weser, O.E., Ross, D.A., et al. (Eds.), Initial Reports of the Deep Sea Drilling Project, 23. U.S. Govt. Printing Office, Washington, D.C., pp. 867–878

Swartz, D.H., Arden, D.D., 1960. Geologic history of the Red Sea area. Bull. Am. Assoc. Pet. Geol. 44, 1621–1637.

Taviani, M., Montagna, P., Rasul, N.M.A., Angeletti, L., Bosworth, W., 2019. Pleistocene coral reef terraces on the Saudi side of the Gulf of Aqaba, Red Sea. In: Rasul, N.M.A., Stewart, I.C.F. (Eds.), Geological Setting, Palaeoenvironment and Archaeology of the Red Sea. Springer Earth System Science Series. Springer Nature, Cham, Switzerland, pp. 341–365.

Tawfik, E., Krebs, W.N., 1994. Environment of Zeit Formation and post-Zeit section (Miocene-Pliocene) in the Gulf of Suez. In: 13th International Diatom Symposium 1994, Italy, pp. 541–554.

Thran, A.C., Dutkiewicz, A., Spence, P., Müller, R.D., 2018. Controls on the global distribution of contourite drifts: insights from an eddy-resolving ocean model. Earth Plant. Sci. Lett. 489, 228–240.

Tian, C., Wang, L., Kaseke, K.F., Bird, B.W., 2018. Stable isotope compositions (δ2H, δ18O and δ17O) of rainfall and snowfall in the Central United States. Sci. Report. 8 art. 6712.

Turab, S.A., Stüwe, K., Stuart, F.M., Cogne, N., Chew, D.M., Robl, J., 2023. A two phase escarpment evolution of the Red Sea margin of southwestern Saudi Arabia. Insights from low-temperature apatite thermochronology. Earth Planet. Sci. Lett. 603 art. 117990.

Vaks, A., Bar-Matthews, M., Ayalon, A., Matthews, A., Frumkin, A., Dayan, U., Halicz, L., Almogi-Labin, A., Schilman, B., 2006. Paleoclimate and location of the border between Mediterranean climate region and the Saharo–Arabian Desert as revealed by speleothems from the northern Negev Desert, Israel. Earth Planet. Sci. Lett. 249, 384–399.

Vaks, A., Bar-Matthews, M., Matthews, A., Ayalon, A., Frumkin, A., 2010. Middle-late Quaternary paleoclimate of northern margins of the Saharan-Arabian Desert: reconstruction from speleothems of Negev Desert, Israel. Quat. Sci. Rev. 29, 2647–2662.

Vaks, A., Woodhead, J., Bar-Matthews, M., Ayalon, A., Cliff, R.A., Zilberman, T., Matthews, A., Frumkin, A., 2013. Pliocene–Pleistocene climate of the northern margin of Saharan–Arabian Desert recorded in speleothems from the Negev Desert, Israel. Earth Planet. Sci. Lett. 368, 88–100.

Viana, A.R., Faugères, J.C., Stow, D.A.V., 1998. Bottom-current-controlled sand deposits - a review of modern shallow- to deep-water environments. Sediment. Geol. 115, 53–80.

Viltres, R., Jónsson, S., Ruch, J., Doubre, C., Reilinger, R., Floyd, M., Ogubazghi, G., 2020. Kinematics and deformation of the southern Red Sea region from GPS observations. Geophys. J. Int. 221, 2143–2154.

Whitmarsh, R.B., Weser, O.E., Ross, D.A., 1974. Initial Reports of the Deep Sea Drilling Project, 23B. U. S. Government Printing Office, Washington, D. C.

Wilckens, H., Eggenhuisen, J.T., Adema, P.H., Hernández-Molina, F.J., Jacinto, R.S., Miramontes, E., 2023. Secondary flow in contour currents controls the formation of moat-drift contourite systems. Commun. Earth & Env. 4 art. 316.

Wilkens, R.H., Westerhold, T., Drury, A.J., Lyle, M., Gorgas, T., Tian, J., 2017. Revisiting the Ceara rise, equatorial Atlantic Ocean: isotope stratigraphy of ODP Leg 154 from 0 to 5 Ma. Clim. Past 13, 779–793.

Wilson, J.W.P., Roberts, G.G., Hoggard, M.J., White, N.J., 2014. Cenozoic epeirogeny of the Arabian Peninsula from drainage modeling. Geochem. Geophys. Geosyst. 15, 3723–3761 doi:3710.1002/2014GC005283.

Winney, B.J., Hammond, R.L., Macasero, W., Flores, B., Boug, A., Biquand, V., Biquand, S., Bruford, M.W., 2004. Crossing the Red Sea: phylogeography of the hamadryas baboon, *Papio hamadryas hamadryas*. Mol. Ecol. 13, 2819–2827.

Zhai, P., Bower, A., 2013. The response of the Red Sea to a strong wind jet near the Tokar Gap in summer. J. Geophys. Res. 118, 422–434 doi:410.1029/2012JC008444.

Zhai, P., Bower, A., 2015. On the crossover of boundary currents in an idealized model of the Red Sea. J. Phys. Oceanogr. 45, 1410–1425.

Zhu, Z., Dennell, R., Huang, W., Wu, Y., Qiu, S., Yang, S., Rao, Z., Hou, Y., Xie, J., Han, J., Ouyang, T., 2018. Hominin occupation of the Chinese Loess Plateau since about 2.1 million years ago. Nature 559, 608–612.